Nano Research

ISSN 1998-0124 CN 11-5974/O4
https://doi.org/10.26599/NR.2026.94909182

Research Article

Entropy-regulated electronic structure of high-entropy Prussian blue analogues drives tumor-selective redox-immunotherapy

Chenyang Bi[1,2], Qingshan Liu[2,3], Xingyan Chen[1], Wei Cao[4], Lei Zhang[4], Hao Zhang[1], Jiahe Yang[1], Yafei Qu[1], Hongda Shi[1], Tao Wei[2,3](✉), Qianwang Chen[1], Evgeny Kataev[3](✉), Dongdong Wang[1,4](✉)

[1] Hefei National Research Center for Physical Sciences at the Microscale, Department of Materials Science and Engineering, University of Science and Technology of China, Hefei 230026, China

[2] State Key Laboratory of Precision and Intelligent Chemistry, University of Science and Technology of China, Hefei 230026, China

[3] Department of Chemistry and Pharmacy, Friedrich Alexander University of Erlangen-Nurnberg, Erlangen 91058, Germany

[4] Department of Pharmacy, The First Affiliated Hospital of USTC, University of Science and Technology of China, Hefei 230001, China

Nano Res., **Just Accepted Manuscript** • https://doi.org/10.26599/NR.2026.94909182

https://www.sciopen.com/journal/1998-0124 on Sep. 9, 2026

© The Authors(s)

Just Accepted

This is a "Just Accepted" manuscript, which has been examined by the peer-review process and has been accepted for publication. A "Just Accepted" manuscript is published online shortly after its acceptance,which is prior to technical editing and formatting and author proofing. Tsinghua University Press (TUP) provides "Just Accepted" as an optional and free service which allows authors to make their results available to the research community as soon as possible after acceptance. After a manuscript has been technically edited and formatted, and the page proofs have been corrected, it will be removed from the "Just Accepted" web site and published officially with volume and article number (e.g., *Nano Research*, **2025**, *18*, 94906990). Please note that technical editing may introduce minor changes to the manuscript text and/or graphics which may affect the content, and all legal disclaimers that apply to the journal pertain. In no event shall TUP be held responsible for errors or consequences arising from the use of any information contained in these "Just Accepted" manuscripts. To cite this anuscript please use its Digital Object Identifier (DOI®),which is identical for all formats of publication.

RESEARCH ARTICLE

Entropy-regulated electronic structure of high-entropy Prussian blue analogues drives tumor-selective redox-immunotherapy

Chenyang Bi[1,2], Qingshan Liu[2,3], Xingyan Chen[1], Wei Cao[4], Lei Zhang[4], Hao Zhang[1], Jiahe Yang[1], Yafei Qu[1], Hongda Shi[1], Tao Wei*[2,3], Qianwang Chen[1], Evgeny Kataev*[3], and Dongdong Wang*[1,4]

1 Hefei National Research Center for Physical Sciences at the Microscale, Department of Materials Science and Engineering, University of Science and Technology of China, Hefei 230026, China
2 State Key Laboratory of Precision and Intelligent Chemistry, University of Science and Technology of China, Hefei 230026, P. R. China.
3 Department of Chemistry and Pharmacy, Friedrich Alexander University of Erlangen-Nurnberg, Erlangen 91058, Germany.
4 Department of Pharmacy, The First Affiliated Hospital of USTC, University of Science and Technology of China, Hefei 230001, China

Received: 24 June 2026; **Revised:** 7 September 2026; **Accepted:** 9 September 2026

Address correspondence to Dongdong Wang, wangdd13@ustc.edu.cn; Evgeny Kataev, evgeny.kataev@fau.de; Tao Wei, taowei2@ustc.edu.cn

Cite this article: *Nano Research*, 2026, 19, 94909182 https://doi.org/10.26599/NR.2026.94909182

Abstract: High configurational entropy can reshape local electronic structures, yet its therapeutic relevance in nanozymes remains largely unexplored. Herein, we demonstrate that the incorporation of multiple transition-metal nodes into ligand-deficient Prussian blue analogues leads to unique asymmetric coordination environments and pronounced intersite electronic reconfiguration, thereby conferring significant catalytic activity. This catalytic electronic rewiring drives a persistent oxidative pressure in tumor cells, rapidly exhausting antioxidant defenses and triggering the accumulation of hydroxyl radicals (•OH). The resulting redox imbalance not only efficiently kills tumor cells but also reprograms the tumor immune microenvironment, promoting dendritic cell maturation, cytotoxic T-cell infiltration, and pro-inflammatory macrophage polarization, leading to strong tumor suppression in vitro and in vivo. This work establishes a direct link between high-entropy-mediated electronic reconfiguration and catalytic immunomodulation, providing a design principle for ligand-deficient high-entropy Prussian blue nanozymes for tumor-specific redox-immunotherapy.

Keywords: Prussian blue analog • nanozyme • high-entropy • ligand-deficient • immunotherapy

Just Accepted

1. Introduction

Structural disorder has emerged as a powerful design principle for tuning catalytic reactivity at the atomic scale.[1] High-entropy materials, featuring stochastic occupation of multiple elements within a single crystallographic framework, enable unique electronic reconfiguration that fundamentally alters adsorption energetics, charge redistribution, and intermediate kinetics.[2,3] Such high-entropy-driven effects have stimulated extensive interest in catalysis and energy conversion, where configurational disorder can optimize reaction pathways and enhance catalytic robustness.[4-6] Despite these advances, the application of high-entropy-regulated catalytic behavior to biologically relevant systems remains largely unexplored. Nanozymes provide a promising bridge between catalytic materials and biological regulation by directly intervening in cellular redox processes.[7-10] Although tumor cells maintain a highly adaptive redox buffering network, primarily via elevated intracellular GSH levels and aberrant peroxide metabolism, to resist oxidative stress,[11,12] catalytic disruption of this balance has emerged as an effective therapeutic strategy.[13-16] For instance, chemodynamic therapy employs peroxidase-like nanozymes to convert endogenous H_2O_2 into cytotoxic •OH, inducing tumor cell death.[17-20] However, most nanozymes rely on structurally ordered active sites with limited electronic tunability, resulting in insufficient catalytic efficiency and redox perturbation in the complex tumor microenvironment.

Introducing high configurational entropy into nanozyme architectures offers a strategy to overcome these limitations. The stochastic distribution of multiple metal centers induces pronounced local lattice distortion, asymmetric coordination environments, and intensified electronic interactions among neighboring catalytic sites.[21,22] These features are particularly relevant for multistep redox transformations that require balanced intermediate adsorption and conversion energetics.[23] However, implementing such high-entropy regulation in biocompatible nanozymes remains challenging, particularly when precise control over coordination unsaturation is needed. Prussian blue analogues (PBAs) represent an attractive scaffold for addressing this challenge,[24,25] as their cyanometallic framework allows the incorporation of multiple transition-metal nodes and controlled ligand vacancies.[26,27] Distinct from conventional defect

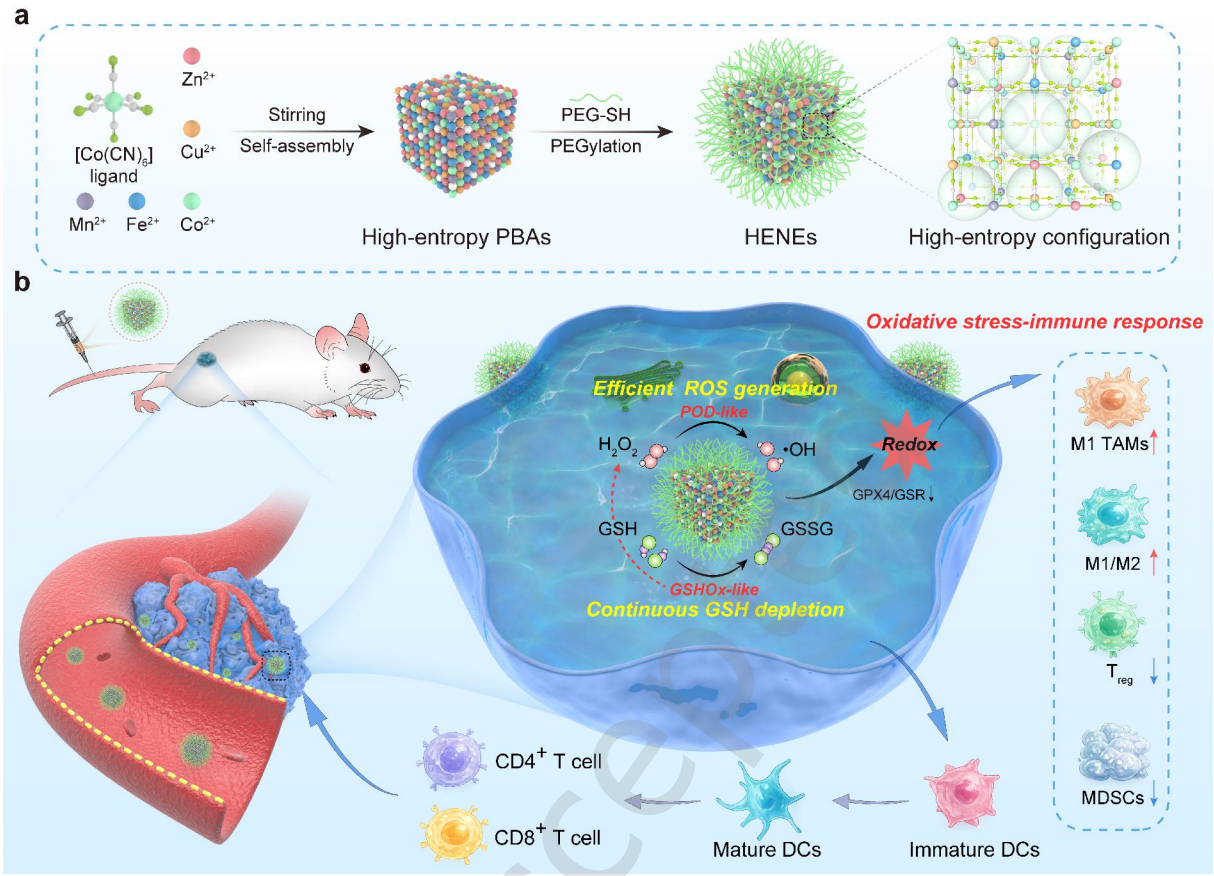


Figure 1. a) Illustration of the self-assembly process of PBA-based high-entropy nanozymes from five types of transition metal species (Mn, Fe, Co, Cu, and Zn) and $[Co(CN)_6]$ bridging ligands, followed by PEGylation. **b)** Accumulation of HENEs in solid tumors after intravenous injection, with cascade enzymatic activity for continuous GSH depletion and efficient reactive oxygen species (ROS) generation, further triggering immunogenic modulation within the tumor microenvironment through self-amplified oxidative stress induced by HENEs and realizing in vivo tumor-specific enzymatic therapy.

engineering that creates isolated unsaturated sites, coupling ligand deficiency with high-entropy configuration generates a synergistically disordered microenvironment, integrating configurational entropy and coordination vacancies to promote collective electronic redistribution.[28,29] Such a dual-disorder effect is expected to facilitate synergistic redox catalysis, enabling concurrent glutathione oxidation and peroxide activation under tumor microenvironment conditions. Despite the growing interest in high-entropy Prussian blue analogues, the mechanistic relationship between configurational entropy, electronic structure, and catalytic activity remains largely unexplored.[30,31]

In addition to direct oxidative damage, persistent redox perturbation is increasingly recognized as a key regulator of the tumor immune microenvironment.[12] Sustained oxidative stress can weaken immunosuppressive signaling and reprogram infiltrating immune cells, thereby reshaping the immune landscape. In particular, redox imbalance is closely linked to macrophage polarization, dendritic cell activation, and T-cell-mediated immune responses, highlighting the intrinsic connection between redox homeostasis and antitumor immunity.[32,33] In addition, transition metal ions are emerging as critical modulators of immune processes. Through catalytic regulation of ROS and redox-sensitive biomolecules, metal-dependent redox activity can influence immune signaling pathways.[34,35] Such metal-immune interactions provide a basis for coupling catalytic chemistry with immunological outcomes, particularly in multimetal systems.[36]

In this study, we propose a strategy that couples high configurational entropy with ligand vacancies to engineer a dual-disordered catalytic microenvironment in Prussian blue analogue nanozymes (HENEs) by integrating Mn, Fe, Co, Cu, and Zn within a single cyanometallic framework (**Figure 1a**). We show that high-entropy-mediated electronic reconfiguration significantly enhances glutathione oxidase-like (GSHOx-like) and peroxidase-like (POD-like) activities, driving antioxidant depletion and sustained hydroxyl radical generation. This catalytic redox rewiring transforms immune-cold tumors into immune-reactive states, characterized by enhanced dendritic-cell maturation, cytotoxic T-cell infiltration, and pro-inflammatory macrophage polarization, ultimately leading to potent tumor suppression in vitro and in vivo (**Figure 1b**). These findings establish high-entropy nanozymes as effective platforms for regulating biological redox catalysis and link high-entropy electronic reconfiguration to redox-immunotherapy.

Just Accepted

2. Experimental

2.1 Materials.

Potassium hexacyanocobaltate ($K_3[Co(CN)_6]$), anhydrous ferrous chloride ($FeCl_2$), cupric chloride dihydrate ($CuCl_2 \cdot 2H_2O$), cobalt chloride hexahydrate ($CoCl_2 \cdot 6H_2O$), manganese chloride tetrahydrate ($MnCl_2 \cdot 4H_2O$), zinc chloride ($ZnCl_2$), and polyvinylpyrrolidone (PVP, K-30) were purchased from Sinopharm Group (Shanghai, China). mPEG-SH (M_w = 2000) was obtained from Laysan Bio Inc. All chemicals were used as received without further purification.

2.2 Synthesis of PBA-based nanozymes.

For the preparation of HENEs, $K_3[Co(CN)_6]$ (67.8 mg) was dispersed in deionized water (10 mL). Deionized water was used to prepare metal salt solutions with an equal concentration of 0.3 mM, including $FeCl_2$, $MnCl_2$, $ZnCl_2$, $CoCl_2$, and $CuCl_2$. Thereafter, the above metal salt solutions (10 mL in total) were added to the mixed solution in turn with PVP (15 mg/mL) as a surfactant under magnetic stirring. The mixture was kept at 90 ℃ for 12 h to allow for a complete reaction. After cooling to room temperature, mPEG-SH (60 mg) was added and stirred for 12 h to obtain HENEs. The preparation methods for MENEs and LENEs were similar, except that the types of metal salt solutions were different, but the total concentration and volume were the same. All products were collected by centrifugation (12840 g, 20 min) and washed three times with deionized water for subsequent characterization. Specifically, HENEs refer to high-entropy nanozymes in which the M_a sites are co-occupied by five transition metals (Mn, Fe, Co, Cu, and Zn). MENEs refer to medium-entropy nanozymes in which the M_a sites are co-occupied by four of these five metals. For example, MENEs-Cu denotes that the M_a sites contain Mn, Fe, Co, and Zn, while Cu is excluded. LENEs denote low-entropy nanozymes in which the M_a sites are occupied solely by Co.

2.3 Characterizations.

The values of metal contents were measured by an inductively coupled plasma-atomic emission spectrometer (iCAP 7400). Transmission electron microscopy (TEM) images were taken with a transmission electron microscope (Hitachi 7650). The high-angle annular dark-field scanning transmission electron microscopy (HAADF-STEM) and corresponding energy dispersive spectroscopy (EDS) mapping analyses were acquired on a high-resolution transmission electron microscope (Talos F200X). Scanning electron microscopy (SEM) images were measured on a field emission scanning electron microscope (GeminiSEM 450). Powder X-ray diffraction (XRD) patterns were acquired by the multifunctional rotating-anode X-ray diffractometer (Rigaku miniflex600). Lattice stripe image analysis was executed on a field emission high-resolution transmission electron microscopy (JEM-F200). The C and N K-edge near-edge X-ray absorption fine structures (NEXAFS) measurements were performed using the soft X-ray magnetic circular dichroism (XMCD) experimental station at the National Synchrotron Radiation Laboratory (NSRL) at the University of Science and Technology of China. Zeta potential and size distribution analyses were performed on a Malvern Nano-ZS ZEN3600 Particle Sizer. Fourier transform infrared spectroscopy (FT-IR) was obtained on a Fourier transform infrared spectrometer (Nicolet 8700). Ultraviolet-visible (UV-vis) absorption spectra were measured on a UV-visible-near infrared Spectrophotometer (SHIMADZU, UV-2600i). Fluorescence spectra were measured on a multifunctional microplate reader. Nuclear magnetic resonance hydrogen spectra (^{1}H NMR) were collected with a superconducting Fourier nuclear magnetic resonance spectrometer, and D_2O was used as the deuterated solvent. X-ray photoelectron spectroscopy (XPS) analysis was performed on Thermo Scientific ESCALAB 250Xi X-ray photoelectron spectrometer. TGA analysis was performed on the Thermal Gravimetric Analyzer TG 209F1.

3. Results and Discussion

3.1 Preparation and morphological characterization.

To construct a catalytically disordered multimetal framework, Prussian blue analogue nanocubes with the composition $Mn_{0.21}Fe_{0.26}Co_{0.14}Cu_{0.22}Zn_{0.17}[Co(CN)_6]_{2/3}\square_{1/3}$ ($\square$ denotes intrinsic $[Co(CN)_6]$ vacancies) were synthesized through a mild self-assembly process and subsequently modified with PEG, affording high-entropy nanozymes (HENEs). The intrinsic one-third ligand deficiency of the Prussian blue analogue lattice creates abundant coordination-unsaturated metal sites, providing a structurally permissive scaffold for accommodating multiple transition-metal species while simultaneously establishing local coordination asymmetry.[26] As illustrated in **Figure 1a**, the spontaneous coordination of Mn, Fe, Co, Cu, and Zn with the nitrogen terminals of $[Co(CN)_6]$ units under aqueous conditions leads to the formation of a multimetallic cyanometallic framework. Mn, Fe, Co, Cu, and Zn were chosen because their comparable ionic sizes favor homogeneous incorporation into the PBA lattice, while their distinct electronic configurations provide diverse local electronic environments. The coexistence of multiple metal species within this ligand-deficient lattice introduces substantial configurational disorder, which is expected to promote local electronic redistribution and intersite coupling among neighboring catalytic centers. Surface functionalization with mPEG-SH was subsequently introduced through metal-thiol coordination to improve the colloidal stability and physiological compatibility.[37,38] To clarify the role of high configurational entropy in regulating catalytic behavior, a series of medium-entropy nanozymes (MENEs), each lacking one metal component, together with a low-entropy counterpart containing only Co at the M_a sites (LENEs), were prepared as control systems. The intrinsic ligand-deficient PBA framework provides a common coordination-unsaturated environment across the entropy series, while increasing configurational entropy introduces additional local coordination disorder and electronic heterogeneity among the metal sites. This entropy-gradient model enables direct evaluation of how multimetal-induced structural disorder influences electronic reconfiguration and catalytic redox activity.

The structural basis of high-entropy-induced catalytic regulation was first established by quantifying the configurational disorder of the multimetallic framework. As illustrated in **Figure 1a**, five transition metal species (Mn,

Not Peer-reviewed

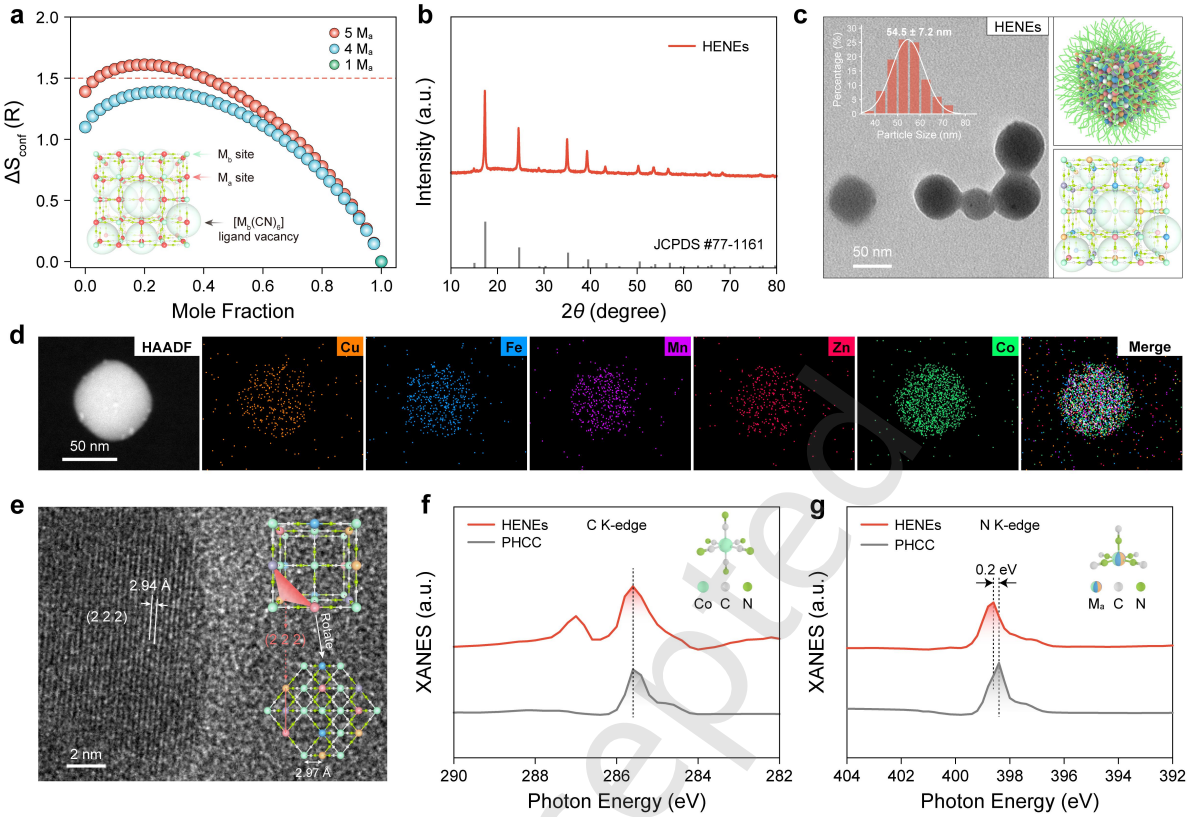


Figure 2. a) Configurational entropy (ΔS_{conf}) of M_a sites with varying numbers of transition metal species in PBA-based nanozymes. Illustration shows the $[M_b(CN)_6]$ ligand vacancy, M_a and M_b site of $(M_a)_3[M_b(CN)_6]_2$. **b)** PXRD patterns of HENEs **c)** TEM image of HENEs, along with statistical analysis of the average particle size from one hundred nanoparticles. The illustration shows the surface microenvironment and crystal structures of HENEs. **d)** HAADF-STEM image of HENEs and corresponding EDS elemental mapping of high-entropy species (Cu, Fe, Mn, Zn, and Co). **e)** HR-TEM image of HENEs; the inset shows the (222) crystal planes of the HENEs. **f)** C K-edge NEXAFS spectra of HENEs, with the structural model of the bridging ligand shown in the inset. **g)** N K-edge NEXAFS spectra of HENEs, and the coordination structure of high entropy species.

Fe, Co, Cu, and Zn) statistically occupy the coordination-unsaturated M_a sites within the ligand-deficient lattice. On the basis of inductively coupled plasma atomic emission spectrometry (ICP-AES) measurements and statistical thermodynamic analysis,[39] the configurational entropy (ΔS_{conf}) of HENEs was calculated to be 1.59R, exceeding the threshold for high-entropy systems (ΔS_{conf} > 1.5R) (**Figure 2a**, **Table S1**, and **Formula S1**). In contrast, the entropy values of the medium- and low-entropy controls fell within their respective regimes, with MENEs-Cu exhibiting a representative ΔS_{conf} of 1.25R. These results confirm the successful construction of an entropy-gradient model for systematically evaluating high-entropy-dependent catalytic behavior. Powder X-ray diffraction (PXRD) patterns revealed that HENEs and all control samples retained the characteristic crystalline structure of the Prussian blue analogue $Co_3[Co(CN)_6]_2$ (JCPDS #77-1161), indicating that the introduction of multiple metal species does not disrupt long-range lattice ordering (**Figure 2b** and **Figure S1**). This structural preservation is essential, as it enables the modulation of local coordination environments without compromising overall framework integrity.

Electron microscopy further revealed that HENEs possess a uniform round-cubic morphology with an average particle size of 54.5 nm, as determined by statistical analysis of 100 nanoparticles (**Figure 2c** and **Figures S2-4**), a size regime favorable for systemic administration. High-angle annular dark-field scanning transmission electron microscopy (HAADF-STEM) combined with elemental mapping demonstrated a homogeneous spatial distribution of Mn, Fe, Co, Cu, and Zn throughout individual nanocubes (**Figure 2d**), excluding phase segregation and supporting the formation of a genuine atomic-level multimetallic configuration. High-resolution transmission electron microscopy (HR-TEM) revealed a lattice spacing of 2.94 Å, corresponding to the (222) crystallographic planes of the parent Prussian blue analogue structure (**Figure 2e** and **Figure S5**). Together with PXRD analysis, those observations confirm that high-entropy incorporation occurs within the preserved cyanometallic lattice rather than through structural reconstruction. More importantly, the intrinsic one-third vacancy fraction of $[Co(CN)_6]$ sites creates abundant coordination-unsaturated metal sites, providing the structural basis for local electronic heterogeneity and high-entropy-dependent redox regulation.

3.2 Structural characterization

Just Accepted

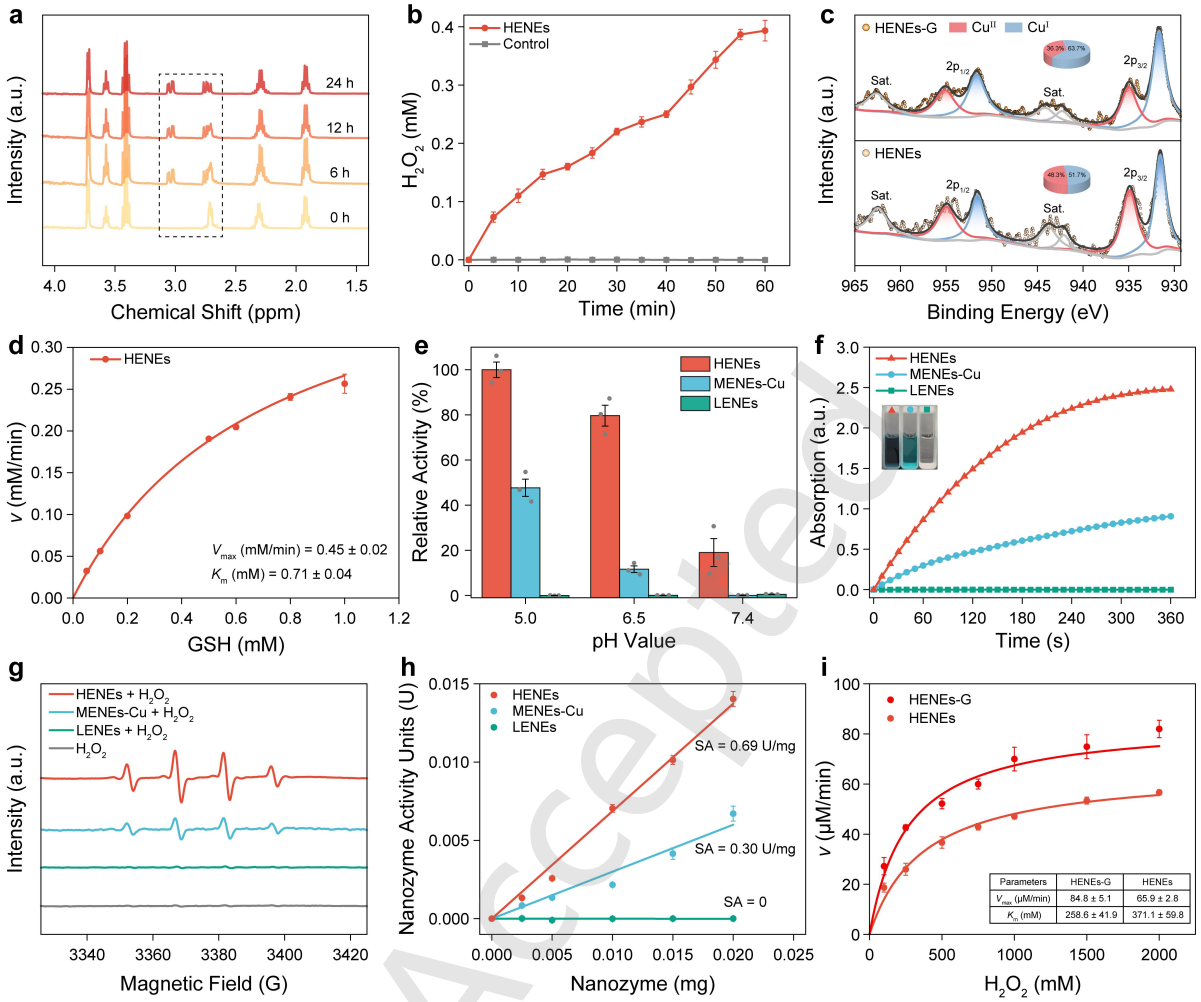


Figure 3. a) ^{1}H NMR analysis during GSH depletion at predetermined time points with HENEs. **b)** Generation of H_2O_2 during the GSH depletion process with HENEs. **c)** XPS analysis of Cu species in HENEs and HENEs-G. The inset shows the ratio of monovalent copper to divalent copper. **d)** Michaelis-Menten curve of the GSHOx-like activity of HENEs. **e)** POD-like activities of LENEs, MENEs-Cu, and HENEs under various physiological conditions. The reactions were carried out in NaAc-HAc buffer (200 mM). **f)** TMB-based colorimetric reactions with LENEs, MENEs-Cu, and HENEs in the presence of H_2O_2 in NaAc-HAc buffer (pH 5.0). The inset shows the blue color of oxidized TMB after 360 s. **g)** ESR spectra for the detection of •OH radicals in different treatment groups. **h)** Specific activity analysis of LENEs, MENEs-Cu, and HENEs. **i)** Michaelis-Menten curves of POD-like activities of HENEs and HENEs-G. Data are presented as the mean ± s.e.m. from three independent experiments (n = 3).

Just Accepted

To further probe the local coordination environments underlying high-entropy-induced electronic reconfiguration, near-edge X-ray absorption fine structure (NEXAFS) spectroscopy was performed. In the C K-edge spectra, HENEs exhibited a peak centered at 289.20 eV, which is identical to that of the ligand precursor, indicating that the carbon-terminal coordination environment of the $[Co(CN)_6]$ units remains structurally preserved after framework assembly (**Figure 2f** and **Figure S6a**). In contrast, the N K-edge spectra displayed a distinct positive shift of approximately 0.2 eV relative to that of the precursor (**Figure 2g** and **Figure S6b**), indicating electron donation from the nitrogen terminals to coordinated transition-metal centers.[40] This spectral evolution confirms the establishment of strong metal-nitrogen coordination interactions and suggests pronounced local electronic redistribution within the multimetallic lattice. These results verify that the ligand-deficient framework accommodates the simultaneous coordination of Mn, Fe, Co, Cu, and Zn at the M_a sites while preserving the overall cyanometallic scaffold. More importantly, such asymmetric multimetal coordination generates electronically heterogeneous local environments, providing direct structural evidence for the high-entropy-induced intersite electronic reconfiguration proposed to govern catalytic redox regulation.

Dynamic light scattering measurements revealed that HENEs possess a hydrodynamic diameter of 107.5 ± 1.6 nm with a narrow size distribution (PDI = 0.09) and a zeta potential of -11.7 mV (**Figure S7**), indicating good colloidal dispersibility. The enlarged hydrodynamic size relative to TEM measurements is consistent with surface PEG hydration.[41] Successful PEGylation was further confirmed

by Fourier transform infrared spectroscopy (FT-IR) and thermogravimetric analysis (TGA), which identified characteristic PEG-associated vibrational signals and a PEG content of approximately 4.7 wt% (**Figures S8-9**).[42] Time-dependent DLS measurements further demonstrated excellent colloidal stability, with negligible size variation over 15 days of storage (**Figure S10**). These interfacial characteristics ensure that the high-entropy-engineered nanostructures remain stably dispersed under physiological conditions for subsequent biological evaluation.

3.3 Cascade multi-enzymatic activity.

Given the multivalent nature of transition-metal centers, we next examined whether the high-entropy configuration could promote glutathione oxidation through cooperative redox regulation.[43-45] ^{1}H NMR spectra revealed the progressive conversion of GSH into GSSG in the presence of HENEs (**Figure 3a**), and the final spectral profile closely matched that of commercial GSSG (**Figure S11**). This transformation was further corroborated by quantitative measurements of GSH depletion and GSSG accumulation using a glutathione detection kit (**Figure S12**). Notably, concurrent H_2O_2 generation was detected during the reaction, reaching approximately 0.4 mM within 1 h (**Figure 3b**), confirming that HENEs possess pronounced GSHOx-like activity. To gain mechanistic insight into this catalytic behavior, X-ray photoelectron spectroscopy (XPS) analysis was performed before and after the reaction with GSH. Following glutathione oxidation, the proportion of Cu^I increased from 51.7% to 63.7%, whereas the valence distributions of the other metal species remained largely unchanged (**Figure 3c** and **Figure S13**). This selective valence evolution suggests that Cu-associated centers play a prominent role in the high-entropy-enabled redox regulation process.

The contribution of high configurational entropy to glutathione oxidation was further assessed by comparing HENEs with their medium- and low-entropy counterparts. After incubation with GSH for 6 h, DTNB analysis showed complete disappearance of the characteristic GSH absorption peak at 412 nm in the HENEs system, whereas substantial residual GSH remained in both MENEs and LENEs (**Figure S14**). In particular, the absence of Cu in MENEs-Cu, together with the loss of catalytic activity, further supports the important role of Cu-mediated multimetal cooperation in promoting glutathione oxidation. Kinetic analysis yielded a Michaelis-Menten constant (K_m) of 0.71 ± 0.04 mM and a maximum initial velocity (V_{max}) of 0.45 ± 0.02 mM/min (**Figure 3d**), highlighting the superior GSHOx-like performance of HENEs. Collectively, these results suggest that although Cu plays a key role in GSH oxidation, the catalytic activity is not governed by an isolated metal center. Instead, the diverse metal sites collectively contribute to the high-entropy catalytic microenvironment, where intensified intersite electronic coupling promotes GSH oxidation and efficient intracellular antioxidant depletion.

Transition metal species can trigger Fenton or Fenton-like reactions, inducing the decomposition of H_2O_2 to produce •OH.[46-49] To evaluate the peroxide activation capability, we first employed 3,3',5,5'-tetramethylbenzidine (TMB) as a chromogenic substrate in the presence of H_2O_2. The time-dependent absorbance evolution revealed that HENEs induced markedly stronger TMB oxidation than both MENEs and LENEs (**Figure S15**). The catalytic activities of the different medium-entropy nanozymes also varied, indicating that the enhanced catalytic activity originates primarily from entropy-induced electronic regulation rather than a simple compositional superposition of multiple metals. Next, we systematically evaluated the POD-like activity of HENEs, and MENEs-Cu were the representative medium-entropy nanozymes. The catalytic behavior of HENEs was further examined under different pH conditions to mimic tumor-relevant acidic microenvironments and physiological environments. As shown in **Figure 3e**, HENEs exhibited pronounced catalytic activity under acidic conditions (pH 5.0 and 6.5), whereas the oxidative activity was substantially suppressed at neutral pH. This pH-dependent activation behavior suggests that the high-entropy configuration enables environment-responsive modulation of peroxide activation, thereby favoring tumor-selective reactivity. In addition, the relatively elevated H_2O_2 and GSH levels in tumors provide favorable substrates for HENEs-mediated redox reactions, thereby contributing to their tumor-selective catalytic activity. Consistently, TMB oxidation produced an intense blue coloration under acidic conditions for HENEs, whereas only weak or negligible color development was observed for MENEs-Cu and LENEs (**Figure 3f**). To verify the generation of reactive oxygen species, terephthalic acid (TA) fluorescence probing and electron spin resonance (ESR) measurements were performed. Both techniques confirmed the efficient formation of hydroxyl radicals in the HENEs system, with significantly stronger signal intensities than those in the control groups (**Figure 3g** and **Figure S16**). Quantitative enzymatic analysis further revealed that the specific activity of HENEs reached 0.69 U mg^{-1}, approximately two-fold higher than that of MENEs-Cu (0.30 U mg^{-1}), whereas LENEs exhibited negligible activity (**Figure 3h**).[50] This enhancement highlights that peroxide activation is strongly governed by the ligand-deficient high-entropy configuration, where multimetal electronic reconfiguration facilitates efficient redox conversion of H_2O_2 into reactive oxygen species, enabling sustained oxidative pressure under tumor-relevant conditions.

The kinetic parameters of POD-like activity were further evaluated for both HENEs and the post-reaction Cu^I-enriched state (denoted as HENEs-G) (**Figure 3i**). Both systems exhibited typical Michaelis-Menten behavior, confirming their enzyme-like catalytic characteristics. Notably, HENEs-G displayed altered kinetic features compared with pristine HENEs, including a lower apparent K_m (258.6 ± 41.9 mM) and an increased V_{max} (84.8 ± 5.1 μM min^{-1}), indicating that Cu valence-state evolution during the catalytic process is closely associated with the modulation of peroxide activation kinetics. This trend was further supported by TMB oxidation assays (**Figure S17**), which

Just Accepted

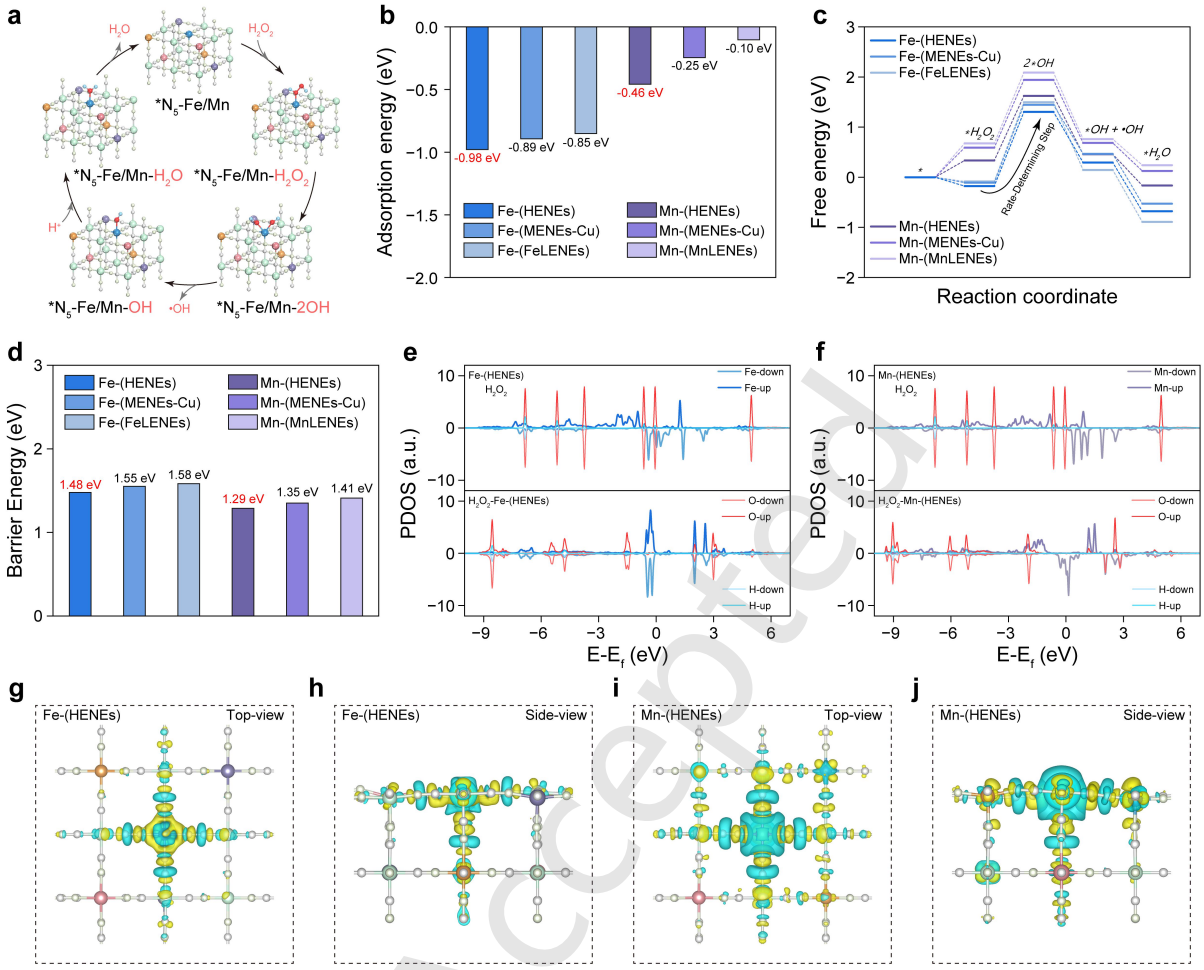


Figure 4. **a)** Schematic illustration of the catalytic mechanism of the POD-like reaction on Fe/Mn-N_5 catalytic sites o HENEs. **b)** Calculated energy of H_2O_2 adsorption on the Fe/Mn-N_5 catalytic sites of PBA-based nanozymes with different entropy values. Fe-(HENEs) represent high-entropy nanozymes with Fe as the active site, Fe-(MENEs-Cu) represents medium-entropy nanozymes (without Cu species at the M_a sites) with Fe as the active site, and Fe-(FeLENEs) represents low-entropy nanozymes (merely with Fe species at the M_a sites) with Fe as the active site.**c)** Corresponding free energy diagram for the POD-like reaction on Fe/Mn-N_5 catalytic sites of PBA-based nanozymes with different entropy values. **d**] Free energy in the homolysis of hydrogen peroxide molecules on Fe/Mn-N_5 catalytic sites of PBA-based nanozymes with different entropy values. **e-f)** PDOS before and after hydrogen peroxide binding to the Fe-N_5 and the Mn-N_5 catalytic sites o HENEs. **g-j)** Electron density difference plots of the Fe-N_5 and Mn-N_5 catalytic sites of HENEs, where the yellow and blue parts represent gaining and losing electrons, respectively.

consistently reflected enhanced catalytic turnover after reaction-induced electronic restructuring. Moreover, kinetic analysis revealed that H_2O_2-dependent reaction rates did not reach saturation at a 10 mM substrate concentration, suggesting the presence of a broad distribution of energetically accessible catalytic sites within the high-entropy framework. In contrast, at elevated substrate concentrations (2 M H_2O_2), a pronounced increase in specific activity was observed for HENEs, exhibiting an ~13-fold increase relative to MENEs-Cu, significantly exceeding the activity difference observed under low-substrate conditions (**Figure S18**). At low H_2O_2 concentrations, the catalytic sites are not fully saturated, whereas under saturating conditions, the enhanced accessibility of catalytic sites in HENEs becomes more evident, resulting in substantially higher activity. Together, these results indicate that the catalytic behavior of HENEs is governed by a highly disordered multimetallic environment, where high-entropy-induced active centers enable tunable substrate utilization and sustained peroxide activation under varying reaction conditions.

High-entropy-induced electronic reconfiguration among multiple transition-metal centers promotes dynamic valence-state interconversion, thereby facilitating efficient redox relay across adjacent catalytic sites. Such multivalent cooperation accelerates the POD-like conversion of H_2O_2 into highly reactive •OH while simultaneously driving glutathione oxidation, resulting in rapid antioxidant exhaustion and amplified oxidative pressure.[51,52] The GSHOx-like activity of HENEs continuously replenishes the intracellular H_2O_2 pool, which, together with endogenous tumor-derived H_2O_2, sustains subsequent •OH generation

Just Accepted

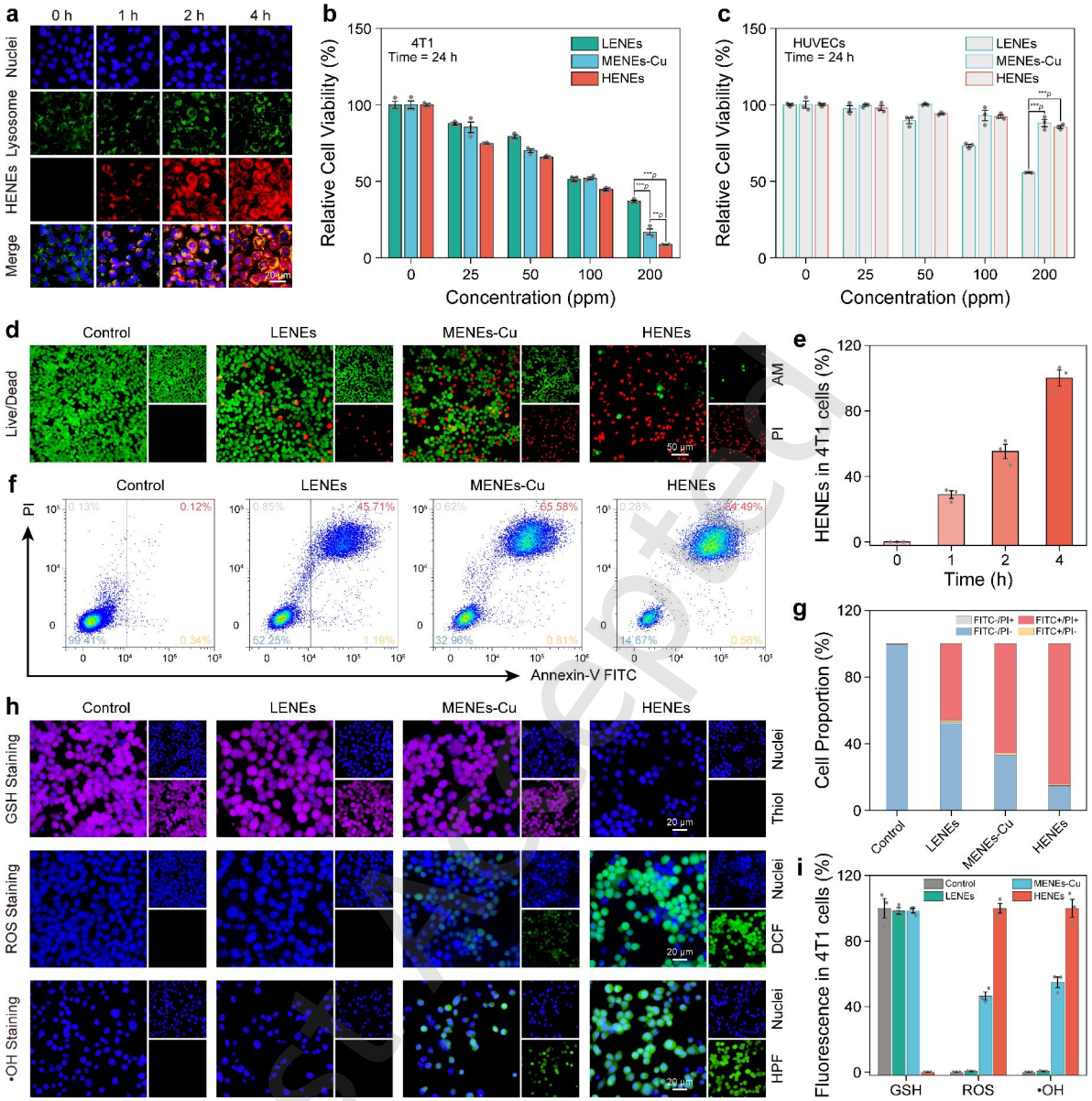


Figure 5. a) Lysosomal endocytosis of HENEs in tumor cells at predetermined time points. **b)** Relative cell viability o cancerous 4T1 cells after treatment with LENEs, MENEs-Cu, and HENEs for 24 h. **c)** Relative cell viability of normal HUVECs after treatment with LENEs, MENEs-Cu, and HENEs for 24 h. **d)** Live and dead staining of tumor cells after different treatments. **e)** Relative quantification of HENEs-Cy5.5 in 4T1 cells. **f)** Apoptosis analysis of tumor cells after different treatments using flow cytometry. **g)** Flow cytometric analysis of 4T1 cells in different treatment groups. **h)** Fluorescence images of GSH, ROS and •OH staining in 4T1 cells with different treatments. **i)** Relative quantification of intracellular GSH ROS and •OH levels in 4T1 cells. Data are presented as mean ± s.e.m. from three independent experiments (n = 3).

from POD-like activity and establishes a dynamically coupled redox cascade. More importantly, the GSHOx-like and POD-like activities of HENEs are coupled through dynamic redox cycling of multiple metal centers. GSH oxidation reduces Cu^{II} to Cu^{I}, while H_2O_2 activation involves electron transfer and valence-state changes at redox-active metal centers. The high-entropy-induced electronic heterogeneity facilitates inter-site electron redistribution, coupling GSH depletion with H_2O_2 activation and •OH generation, thereby sustaining catalytic activity and amplifying oxidative stress. This coupled catalytic process enables persistent disruption of intracellular redox homeostasis, highlighting how structural disorder within a high-entropy configuration translates into enhanced cascade catalytic performance.

3.4 Density functional theory calculations

To elucidate how configurational entropy governs peroxide activation, density functional theory calculations were performed using representative entropy-gradient structural models.[53] The calculations identified Fe- and Mn-associated coordination sites as the preferred centers for H_2O_2 adsorption and activation within HENEs. As shown in **Figures 4a-b**, HENEs exhibited substantially stronger H_2O_2 adsorption than MENEs-Cu and LENEs, with adsorption

Just Accepted

energies of -0.98 and -0.46 eV at the Fe and Mn sites, respectively, indicating that the enhanced substrate affinity arises from high-entropy-modulated local coordination environments. Following adsorption, H_2O_2 undergoes homolytic dissociation into *2OH intermediates prior to hydroxyl radical release, with this bond cleavage step constituting the rate-determining process. Notably, the calculated activation barriers at Fe/Mn-N_5 sites in HENEs (1.48 and 1.29 eV, respectively) were markedly lower than those of their medium- and low-entropy counterparts (**Figures 4c-d**), demonstrating that configurational disorder kinetically facilitates peroxide conversion. To probe the electronic origin of this catalytic enhancement, a projected density of states analysis was conducted. Compared with MENEs-Cu and LENEs, Fe/Mn–N_5 sites in HENEs display increased occupation of binding states below the Fermi level together with stronger orbital overlap with adsorbed H_2O_2 (**Figures 4e-f**, and **Figure S19**), indicating reinforced interfacial electronic reconfiguration.[54] Differential charge density analysis further revealed substantial local electron redistribution around Fe/Mn centers within the high-entropy lattice, generating electron-deficient regions favorable for peroxide adsorption and activation (**Figures 4g-j**).[49]

These theoretical results reveal that peroxide activation in HENEs is governed by high-entropy-induced electronic heterogeneity rather than isolated elemental activity. While Fe and Mn serve as the principal reactive centers, the surrounding multimetal coordination environment collectively reshapes local reaction energetics through intersite electronic modulation, thereby lowering the energy barrier for hydroxyl radical generation. This high-entropy-enabled electronic rewiring provides the mechanistic origin of the experimentally observed increase in POD-like activity and sustained oxidative amplification.

3.5 Cascade-amplified oxidative stress and in vitro anti-tumor study

Having established the high-entropy-enabled dual redox catalytic behavior of HENEs, we next investigated whether this catalytic regulation could be effectively activated within the intracellular tumor environment. To track cellular internalization, HENEs were labeled with thiol-functionalized Cy5.5 (Cy5.5-PEG-SH), affording HENEs-Cy5.5. Confocal laser scanning microscopy revealed efficient time-dependent uptake of HENEs-Cy5.5 by 4T1 cells, with fluorescence signals predominantly colocalized with lysosomes (**Figures 5a** and **5e**). This preferential lysosomal localization is particularly significant, as the acidic lysosomal milieu provides an ideal biochemical context for triggering high-entropy-mediated peroxide activation and glutathione oxidation.

To further examine their environment-responsive behavior, HENEs were incubated under physiological (pH 7.4) and lysosome-mimicking conditions (pH 5.0, 10 mM GSH). As shown in **Figure S20**, HENEs retained their structural integrity under physiological conditions for more than 48 h, indicating sufficient extracellular stability for systemic delivery. In contrast, under lysosomal conditions, the nanostructures underwent progressive degradation and gradually transformed into an amorphous state. This selective structural evolution likely facilitates the exposure of coordination-asymmetric multimetal centers, thereby promoting intracellular catalytic activation. Such spatiotemporally regulated behavior ensures that the high-entropy catalytic framework remains largely inert during circulation while becoming selectively activated after lysosomal internalization. This intracellularly triggered redox activation provides the mechanistic basis for tumor-selective disruption of redox homeostasis.

The intracellular catalytic consequences of high-entropy-regulated redox activation were next evaluated in 4T1 tumor cells. MTT assays revealed a pronounced high-entropy-dependent therapeutic response, with HENEs exhibiting the strongest cytotoxicity among all the tested nanozymes (**Figure 5b**). At 200 ppm, HENEs induced 91.41% tumor cell inhibition after 24 h, substantially outperforming both MENEs-Cu and LENEs. This superior therapeutic efficacy is consistent with the sustained oxidative amplification enabled by coupled glutathione depletion and peroxide activation. Importantly, HENEs displayed minimal toxicity toward HUVECs under the same treatment conditions, maintaining cell viability above 85% after 24 h of incubation (**Figure 5c**), indicating favorable selectivity toward tumor-associated redox environments. In contrast to the high-entropy-dependent catalytic behavior observed in tumor cells, normal-cell viability remained largely preserved, supporting the tumor-selective nature of intracellular catalytic activation. Live/dead fluorescence staining further confirmed the markedly enhanced tumoricidal activity of HENEs (**Figure 5d**), while flow cytometric analysis revealed extensive apoptotic progression following treatment. Compared with the control groups, HENEs-treated 4T1 cells showed a pronounced transition from viable to late apoptotic populations, with late apoptosis reaching 84.49% (**Figures 5f-g**), demonstrating that high-entropy-enabled redox disruption efficiently commits tumor cells to irreversible death pathways. To directly probe intracellular redox perturbation, glutathione levels were monitored using ThiolTracker Violet (**Figures 5h-i**). Cells treated with HENEs exhibited a near-complete loss of intracellular thiol fluorescence, whereas MENEs-Cu, LENEs, and PBS-treated controls retained strong signals, indicating the preservation of antioxidant capacity. This dramatic glutathione depletion confirms that the high-entropy catalytic framework effectively dismantles the intracellular redox buffering system.

Consistent with this antioxidant collapse, intracellular ROS measurements using DCFH-DA revealed the highest oxidative burden in the HENEs-treated group, followed by that in the MENEs-Cu group, whereas negligible ROS accumulation was observed in the LENEs and control groups (**Figures 5h-i**). Hydroxyphenyl fluorescein staining further verified substantially elevated hydroxyl radical generation in HENEs-treated cells, directly linking high-entropy-enhanced peroxide activation to intracellular

Just Accepted

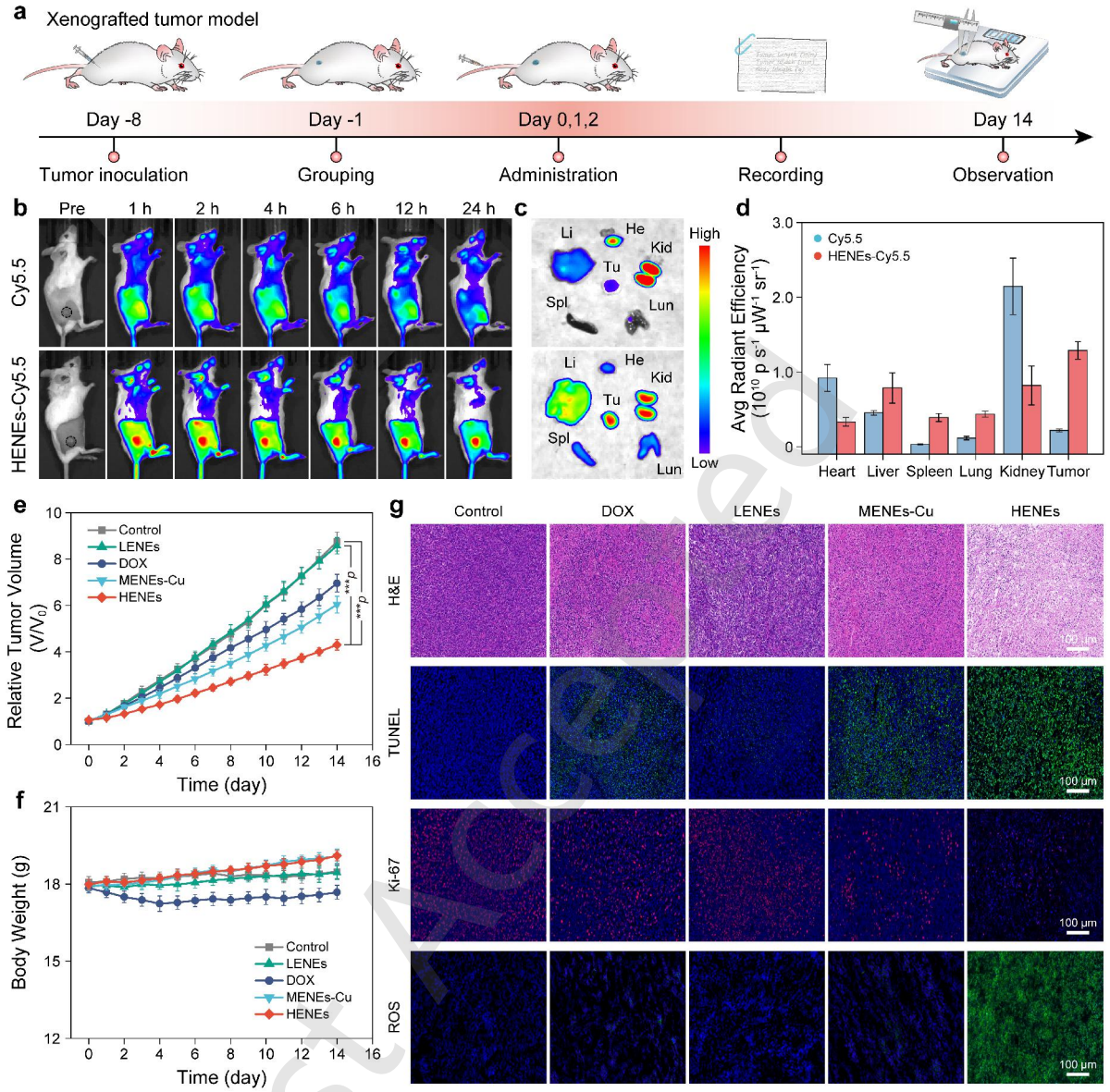


Figure 6. a) Illustration showing the in vivo tumor treatment procedure. **b)** In vivo fluorescence imaging of 4T1 tumor-bearing mice at predetermined time points after intravenous administration of Cy5.5 or HENEs-Cy5.5. **c)** Ex vivo fluorescence imaging of the main organs (heart, liver, spleen, lung, and kidney) and tumor tissues 24 h post-administration. **d)** Corresponding quantitative analysis of the fluorescence intensity of the main organs and tumor tissues. **e)** Average tumor growth curves of 4T1 tumor-bearing mice from different treatment groups. **f)** Average body weight curves during the treatment. **g)** ROS, immunohistochemical and immunofluorescence stainings of representative tumor slices, including H&E staining, TUNEL staining, and Ki-67 staining. Data are presented as the mean ± s.e.m. from five mice (n = 5).

oxidative amplification. Collectively, these results demonstrate that high-entropy-enabled catalytic rewiring translates into efficient intracellular redox disequilibrium, wherein coordinated glutathione exhaustion and sustained hydroxyl radical production drive oxidative collapse and potent tumor cell apoptosis.

3.6 In vivo biosafety study

Encouraged by the high-entropy-dependent redox disruption observed in vitro, we next evaluated whether this catalytic behavior could be translated into effective tumor suppression in vivo using a 4T1 xenografted breast tumor model. The treatment protocol is illustrated in **Figure 6a**. Prior to therapeutic evaluation, the systemic compatibility of HENEs was comprehensively assessed. Hemolysis and coagulation analyses revealed negligible interference with normal blood function even at concentrations up to 800 ppm (**Figure S21**). Longitudinal hematological and biochemical analyses revealed no significant abnormalities in routine blood parameters or liver and kidney function markers over 14 days following intravenous administration (**Figure S22**), indicating favorable systemic tolerance.

To determine whether HENEs could access tumor tissues following systemic delivery, their biodistribution was monitored using Cy5.5-labeled nanozymes. In vivo fluorescence imaging revealed pronounced and sustained

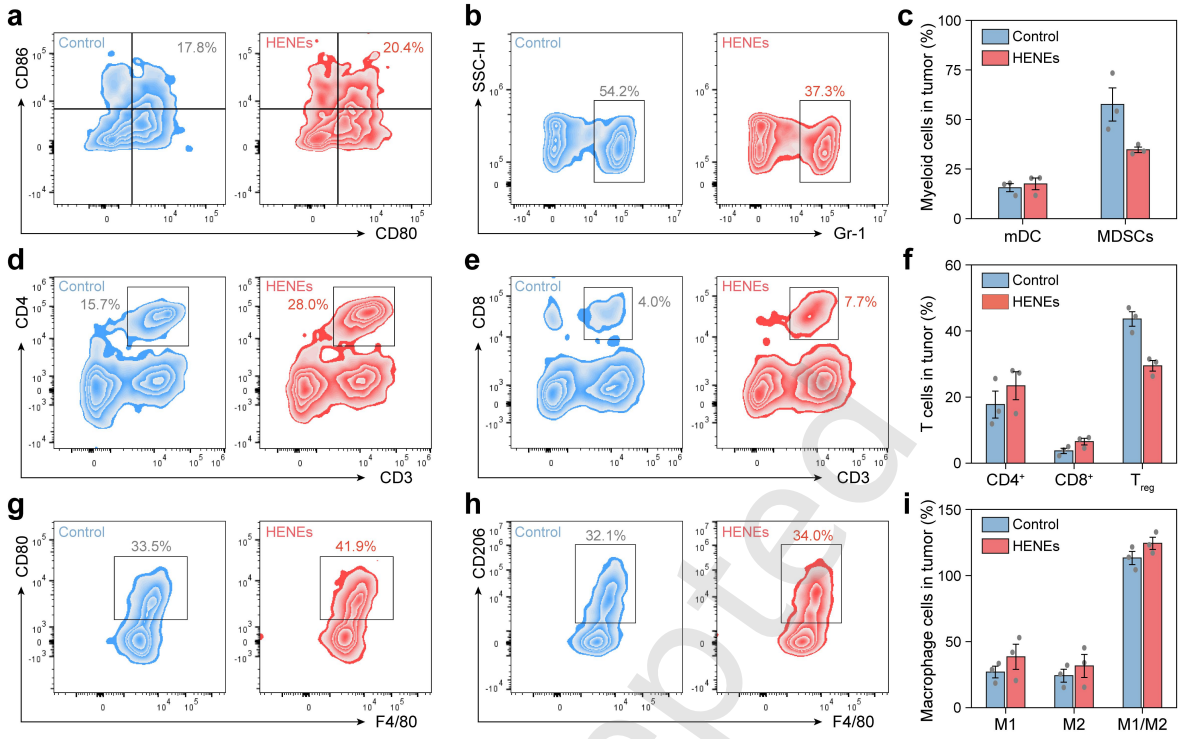


Figure 7. a) Flow cytometric analysis of mature dendritic cells (mDCs) in tumors. **b)** Flow cytometric analysis of MDSCs ir tumors. **c)** Relative populations of myeloid cells in tumors. **d)** Flow cytometric analysis of $CD4^+$ T cells in the tumor. **e)** Flow cytometric analysis of $CD8^+$ T cells in tumors. **f)** Relative populations of T cells in the tumor. **g)** Flow cytometric analysis o M1 macrophages in tumors. **h)** Flow cytometric analysis of M2 macrophages in tumors. **i)** Relative populations o macrophage cells in tumors.

accumulation of HENEs at tumor sites for up to 24 h post-injection, markedly exceeding that of free Cy5.5 controls (**Figure 6b** and **Figure S23**).[55] Ex vivo imaging further confirmed preferential tumor retention relative to that of major organs (**Figures 6c-d**), indicating that the nanoscale high-entropy-engineered framework enables efficient passive enrichment within tumor tissue.

3.7 In vivo anti-tumor study

Following confirmation of tumor accumulation, therapeutic efficacy was evaluated in tumor-bearing Balb/c mice. Animals were randomly assigned to the PBS, DOX, LENEs, MENEs-Cu, and HENEs treatment groups once the tumors reached an average volume of approximately 60 mm^3. Among all tested formulations, HENEs exhibited the most pronounced suppression of tumor progression, with a tumor inhibition rate of 47.1% (**Figure 6e**). In contrast, LENEs showed minimal therapeutic benefit, whereas MENEs-Cu displayed only partial inhibition. Although DOX induced moderate antitumor activity, it was accompanied by substantial body-weight loss during treatment (**Figure 6f**), which is consistent with systemic toxicity.[56,57] In contrast, mice treated with HENEs maintained a stable body weight comparable to that of the PBS controls, further highlighting the favorable therapy enabled by high-entropy-regulated catalytic activation.

The therapeutic superiority of HENEs was further confirmed by endpoint tumor mass analysis, with HENEs-treated mice exhibiting the lowest average tumor weight (**Figure S24**). Histopathological examination revealed no significant structural abnormalities in major organs across all the nanozyme-treated groups (**Figure S25**), supporting excellent in vivo biosafety. Biodistribution quantification further revealed progressive systemic clearance, with HENEs becoming nearly undetectable in circulation and major organs within 7 days post-administration (**Figure S26**). To directly verify in vivo redox disruption, harvested tumor tissues were subjected to biochemical and histological analyses. H&E staining revealed extensive structural destruction in tumors treated with HENEs, while TUNEL staining revealed markedly elevated apoptotic signaling and Ki-67 staining confirmed substantial suppression of proliferative activity (**Figure 6g**). Importantly, HENEs induced pronounced intratumoral glutathione depletion together with robust ROS accumulation (**Figure S27** and **Figure 6g**), whereas these effects were substantially weaker in MENEs-Cu-treated tumors and negligible in LENEs or PBS controls. These findings establish that the high-entropy catalytic framework remains systemically compatible while becoming preferentially activated within tumor tissues, where coordinated glutathione exhaustion and sustained oxidative amplification drive efficient tumor suppression in vivo. This selective redox disequilibrium bridges the mechanistic insights of high-entropy-enabled catalysis with its therapeutic outcome at the biological level.

3.8 Tumor-infiltrating immune cells study

Just Accepted

The immunological consequences of the catalytic redox perturbation induced by HENEs were evaluated, and tumor-infiltrating immune cells were analyzed by flow cytometry. The results revealed general reprogramming of the tumor immune landscape following HENEs treatment (**Figure S28**). Specifically, an increase in mature dendritic cell populations was accompanied by a reduction in immunosuppressive myeloid-derived suppressor cells, indicating the alleviation of tumor-associated immune suppression (**Figures 7a-c**). Concurrently, adaptive immune responses shifted toward an immunologically responsive state, as evidenced by elevated proportions of $CD4^+$ and $CD8^+$ T cells and a decreased level of regulatory T cells (**Figures 7d-f** and **Figure S29**). In addition, macrophage polarization analysis clearly revealed a shift toward the pro-inflammatory M1 phenotype following HENEs intervention (**Figures 7g-i**), suggesting the activation of innate immune responses within the tumor microenvironment. These coordinated immune alterations indicate that HENEs-induced oxidative stress extends beyond direct tumor cell damage and contributes to the remodeling of both innate and adaptive immune responses, thereby reshaping the tumor microenvironment toward a more immunostimulatory state.

3.9 Transcriptomic study

To further elucidate the tumor-level response to high-entropy-induced redox perturbation, transcriptome profiling was performed on tumor tissues harvested after HENEs or PBS treatment. Principal component analysis revealed clear separation between the two groups, indicating that HENEs treatment induces a distinct transcriptional state transition within the tumor microenvironment (**Figure S30**). Differential expression analysis revealed 273 genes whose expression significantly changed ($|\text{fold change}| > 2$, $p < 0.05$), including 74 upregulated genes and 199 downregulated genes (**Figures 8a** and **S31**). Functional enrichment analyses were conducted to interpret these global transcriptional changes. GO and KEGG enrichment results revealed that HENEs-induced gene reprogramming is associated mainly with three interconnected functional modules: cellular proliferation regulation, redox homeostasis, and immune signaling networks (**Figures 8b-c**). In particular, pathways involved in the oxidative stress response, MAPK and PI3K–Akt signaling, cytokine communication, and Toll-like receptor signaling were prominently affected, suggesting a coordinated shift in tumor cell fate regulation and microenvironmental signaling. GSEA further confirmed a global transition toward oxidative stress-dominant and immune-modulatory transcriptional states (**Figure S32**), which is consistent with sustained redox perturbation in tumor tissues. At the gene module level, redox-related signatures included the suppression of the expression of antioxidant defense components such as Ngfr and Mgst2, and the activation of stress-responsive signaling genes such as Map2k6, indicating a weakened glutathione-dependent buffering capacity and increased oxidative susceptibility.[58,59] Concurrently, genes associated with genomic integrity and cellular stress responses (e.g., Trex1, Trim39, and Tm6sf2) exhibited significant expression changes, reflecting an elevated intracellular stress burden.[60-62] Immune-associated transcriptional remodeling, including altered expression of Il1a, Cxcl1, and Fcgrt, were also observed, suggesting the perturbation of tumor immune signaling networks (**Figure 8d**). Protein-protein interaction analysis further highlighted central nodes including Il1a, Hspa1b, and Mrc1, which are closely linked to stress adaptation and redox-immune crosstalk (**Figure S33**).

These transcriptional signatures were validated at the protein and functional levels. Western blot analysis demonstrated that HENEs downregulated the key antioxidant enzymes GSR and GPX4 in 4T1 tumor cells, confirming the disruption of glutathione-dependent redox homeostasis (**Figure S34a**). In addition, cell cycle analysis revealed a significant increase in G1-phase arrest, indicating the suppression of DNA replication and tumor proliferative capacity under sustained oxidative stress (**Figure S34b**). Collectively, these results demonstrate that high-entropy-driven redox perturbation induces a coordinated transcriptomic-to-functional transition characterized by impaired antioxidant defense, an elevated stress response, and suppressed tumor growth.

4. Conclusion

In summary, Prussian blue analogues with intrinsically disordered multimetal active centers exhibit high-entropy-dependent electronic reconfiguration that fundamentally alters their catalytic redox behavior. The resulting high-entropy configuration enables coordinated multimetal redox cycling, leading to the concurrent enhancement of glutathione oxidation and peroxide activation under tumor microenvironment conditions. This high-entropy-driven catalytic behavior establishes a self-sustained oxidative process characterized by the continuous disruption of intracellular redox homeostasis. Importantly, the influence of such persistent redox perturbation extends beyond tumor cell damage, driving broader reprogramming of the tumor immune microenvironment toward a more pro-inflammatory and immunologically responsive state. Overall, these findings show that high-entropy configurations can regulate catalytic electron transfer and couple redox chemistry with immune responses, providing mechanistic insight into tumor redox-immune modulation via catalytic rewiring.

Data availability

All data needed to support the conclusions in the paper are presented in the manuscript and/or the Electronic Supplementary Material.

Acknowledgements

This work was supported by the National Natural Science Foundation of China (22272155, 52373160, 22305242), the Anhui Provincial Natural Science Foundation (2308085MB34), Deutsche Forschungsgemeinschaft (DFG,

Unaccepted

German Research Foundation, KA3444/16-1), the Anhui Clinical Medical Research Transformation Special Project (202304295107020050), and the USTC Bihe Youth Program for Interdisciplinary Innovation (BH-202501). This work was partially carried out at the Instruments Center for Physical Science, University of Science and Technology of China (USTC). The DFT calculations were performed at the Supercomputing Center of USTC. The authors also thank the Soft X-ray Magnetic Circular Dichroism End Station (XMCD) of the National Synchrotron Radiation Laboratory (NSRL) at the USTC for measurements of C and N K-edge XANES.

Declaration of competing interest

The authors declare no conflict of interest.

Author contribution statement

C. Y. B.: Data curation, formal analysis, validation, visualization, writing – original draft. Q. S. L.: Methodology, investigation. X. Y. C.: Data curation, methodology. W. C.: Formal analysis, validation. L. Z.: Investigation, formal analysis. H. Z.: Resources, methodology, formal analysis. J. H. Y.: Investigation, formal analysis. Y. F. Q.: Investigation, formal analysis. H. D. S.: Investigation, formal analysis. T. W.: Formal analysis, funding acquisition, writing – review & editing. Q. W. C.: Formal analysis, writing – review & editing. E. K.: Formal analysis, funding acquisition, writing – review & editing. D. D. W.: Conceptualization, supervision, resources, project administration, writing – review & editing, funding acquisition, methodology. All the authors have approved the final manuscript.

Use of AI statement

None.

References

[1] Wyatt, B. C.; Yang, Y.; Michałowski, P. P.; Parker, T.; Morency, Y.; Urban, F.; Kadagishvili, G.; Tanwar, M.; Muhoza, S. P.; Nemani, S. K. et al. Order-to-disorder transition due to entropy in layered and 2D carbides. *Science* **2025**, *389*, 1054-1058.

[2] Hsu, W.-L.; Tsai, C.-W.; Yeh, A.-C.; Yeh, J.-W. Clarifying the four core effects of high-entropy materials. *Nat. Rev. Chem.* **2024**, *8*, 471-485.

[3] Kar, N.; Skrabalak, S. E. Synthetic methods for high-entropy nanomaterials. *Nature Reviews Materials* **2025**, *10*, 638-653.

[4] Yao, Y.; Dong, Q.; Brozena, A.; Luo, J.; Miao, J.; Chi, M.; Wang, C.; Kevrekidis, I. G.; Ren, Z. J.; Greeley, J. et al. High-entropy nanoparticles: Synthesis-structure-property relationships and data-driven discovery. *Science* **2022**, *376*, eabn3103.

[5] Qi, S.; Zhu, K.; Xu, T.; Zhang, H.; Guo, X.; Wang, J.; Zhang, F.; Zong, X. Water‐Stable High‐Entropy Metal‐Organic Framework Nanosheets for Photocatalytic Hydrogen Production. *Adv. Mater.* **2024**, *36*, 2403328.

[6] Iyyappan, M.; Senthil, C.; Ghosh, D. Entropically Stabilized Compositionally Complex Prussian Blue Analogues in Electrochemical Energy Storage and Catalytic Applications. *Adv. Energy Mater.* **2026**, *16*, e05809.

[7] Gao, L.; Zhuang, J.; Nie, L.; Zhang, J.; Zhang, Y.; Gu, N.; Wang, T.; Feng, J.; Yang, D.; Perrett, S. et al. Intrinsic peroxidase-like activity of ferromagnetic nanoparticles. *Nat. Nanotechnol.* **2007**, *2*, 577-583.

[8] Zhang, R.; Jiang, B.; Fan, K.; Gao, L.; Yan, X. Designing nanozymes for in vivo applications. *Nat. Rev. Bioeng.* **2024**, *2*, 849-868.

[9] Yang, L.; Zhao, Z.; Gai, S.; Zang, P.; Yang, M.; Yu, C.; Gong, H.; Yan, W.; Xie, Y.; Tang, Y. et al. Sulfur Vacancy-Enriched Cu4SnS4−x Nanosheets Enable Synergistic Cuproptosis, Photothermoelectric Catalytic and Immunotherapy. *Angew. Chem. Int. Ed.* **2026**, *65*, e1499416.

[10] Zhu, Y.; Zhao, R.; Feng, L.; Wang, C.; Dong, S.; Zyuzin, M. V.; Timin, A.; Hu, N.; Liu, B.; Yang, P. Dual Nanozyme-Driven PtSn Bimetallic Nanoclusters for Metal-Enhanced Tumor Photothermal and Catalytic Therapy. *ACS Nano* **2023**, *17*, 6833-6848.

[11] Hecht, F.; Zocchi, M.; Alimohammadi, F.; Harris, I. S. Regulation of antioxidants in cancer. *Mol. Cell* **2024**, *84*, 23-33.

[12] Glorieux, C.; Liu, S.; Trachootham, D.; Huang, P. Targeting ROS in cancer: rationale and strategies. *Nat. Rev. Drug Discovery* **2024**, *23*, 583-606.

[13] Xiong, Y.; Xiao, C.; Li, Z.; Yang, X. Engineering nanomedicine for glutathione depletion-augmented cancer therapy. *Chem. Soc. Rev.* **2021**, *50*, 6013-6041.

[14] Hayes, J. D.; Dinkova-Kostova, A. T.; Tew, K. D. Oxidative Stress in Cancer. *Cancer Cell* **2020**, *38*, 167-197.

[15] Zhu, Y.; Wang, X.; Feng, L.; Zhao, R.; Yu, C.; Liu, Y.; Xie, Y.; Liu, B.; Zhou, Y.; Yang, P. Intermetallics triggering pyroptosis and disulfidptosis in cancer cells promote anti-tumor immunity. *Nat. Commun.* **2024**, *15*, 8696.

[16] Zhu, Y.; Hao, Q.; Zhu, H.; Zhao, R.; Feng, L.; He, S.; Wang, W.; He, G.; Liu, B.; Yang, P. Thermoelectric Nanoheterojunction-Mediated Multiple Energy Conversion for Enhanced Cancer Therapy. *ACS Nano* **2024**, *18*, 34257-34271.

[17] Zhang, C.; Bu, W.; Ni, D.; Zhang, S.; Li, Q.; Yao, Z.; Zhang, J.; Yao, H.; Wang, Z.; Shi, J. Synthesis of Iron Nanometallic Glasses and Their Application in Cancer Therapy by a

Just Accepted

Localized Fenton Reaction. *Angew. Chem. Int. Ed.* **2016**, *55*, 2101-2106.

[18] Wang, L.-C.; Chiou, P.-Y.; Hsu, Y.-P.; Lee, C.-L.; Hung, C.-H.; Wu, Y.-H.; Wang, W.-J.; Hsieh, G.-L.; Chen, Y.-C.; Chang, L.-C. et al. Prussian blue analog with separated active sites to catalyze water driven enhanced catalytic treatments. *Nat. Commun.* **2023**, *14*, 4709.

[19] Zhao, P.; Li, H.; Bu, W. A Forward Vision for Chemodynamic Therapy: Issues and Opportunities. *Angew. Chem. Int. Ed.* **2023**, *62*, e202210415.

[20] Zhao, R.; Zhu, Y.; Feng, L.; Liu, B.; Hu, Y.; Zhu, H.; Zhao, Z.; Ding, H.; Gai, S.; Yang, P. Architecture of Vanadium‐Based MXene Dysregulating Tumor Redox Homeostasis for Amplified Nanozyme Catalytic/Photothermal Therapy. *Adv. Mater.* **2024**, *36*, 2307115.

[21] He, L.; Li, M.; Qiu, L.; Ren, X.; Tian, F.; Sheng, J.; Liu, Y.; Luo, M.; Zhou, X.; Yu, Y. et al. Breaking the symmetry of high-entropy alloy surfaces for compressively strain-tuned oxygen reduction reaction. *Nat. Commun.* **2025**, *16*, 10834.

[22] Zhang, T.; Zhao, H.-F.; Chen, Z.-J.; Yang, Q.; Gao, N.; Li, L.; Luo, N.; Zheng, J.; Bao, S.-D.; Peng, J. et al. High-entropy alloy enables multi-path electron synergism and lattice oxygen activation for enhanced oxygen evolution activity. *Nat. Commun.* **2025**, *16*, 3327.

[23] Qian, F.; Peng, L.; Cao, D.; Jiang, W.; Hu, C.; Huang, J.; Zhang, X.; Luo, J.; Chen, S.; Wu, X. et al. Asymmetric active sites originate from high-entropy metal selenides by joule heating to boost electrocatalytic water oxidation. *Joule* **2024**, *8*, 2342-2356.

[24] Huo, M.; Tang, Z.; Wang, L.; Zhang, L.; Guo, H.; Chen, Y.; Gu, P.; Shi, J. Magnesium hexacyanoferrate nanocatalysts attenuate chemodrug-induced cardiotoxicity through an anti-apoptosis mechanism driven by modulation of ferrous iron. *Nat. Commun.* **2022**, *13*, 7778.

[25] Liu, Q.; Zhao, S.; Zhang, Y.; Fang, Q.; Liu, W.; Wu, R.; Wei, G.; Wei, H.; Du, Y. Nanozyme‐Cosmetic Contact Lenses for Ocular Surface Disease Prevention. *Adv. Mater.* **2023**, *35*, 2305555.

[26] Simonov, A.; De baerdemaeker, T.; Boström, H. L. B.; Ríos Gómez, M. L.; Gray, H. J.; Chernyshov, D.; Bosak, A.; Bürgi, H.-B.; Goodwin, A. L. Hidden diversity of vacancy networks in Prussian blue analogues. *Nature* **2020**, *578*, 256-260.

[27] Li, J.; Liu, X.; Tan, L.; Cui, Z.; Yang, X.; Liang, Y.; Li, Z.; Zhu, S.; Zheng, Y.; Yeung, K. W. K. et al. Zinc-doped Prussian blue enhances photothermal clearance of Staphylococcus aureus and promotes tissue repair in infected wounds. *Nat. Commun.* **2019**, *10*, 4490.

[28] Hoffman, R. S. Thallium Toxicity and the Role of Prussian Blue in Therapy. *Toxicol. Rev.* **2012**, *22*, 29-40.

[29] Qin, Z.; Li, Y.; Gu, N. Progress in Applications of Prussian Blue Nanoparticles in Biomedicine. *Adv. Healthcare Mater.* **2018**, *7*, 1800347.

[30] Xing, Y.; Yin, C.; Yin, Y.; Xue, J.; Liu, Y.; Li, J.; Chi, L.; Gu, W. Nanozyme-mediated high-entropy-driven photothermally enhanced tumor catalytic therapy. *Journal of Materials Chemistry B* **2025**, *13*, 7854-7864.

[31] Xing, Y.; Yin, C.; Luo, K.; Yin, Y.; Zhao, P.; Xue, J.; Gu, W. A high-entropy nanozyme-based photothermal-adjuvant in situ nanovaccine for potentiated tumor immunotherapy. *Materials Chemistry Frontiers* **2025**, *9*, 2634-2645.

[32] Liang, X.; Weng, J.; You, Z.; Wang, Y.; Wen, J.; Xia, Z.; Huang, S.; Luo, P.; Cheng, Q. Oxidative stress in cancer: from tumor and microenvironment remodeling to therapeutic frontiers. *Mol. Cancer* **2025**, *24*, 219.

[33] Li, J.; Huang, C.; Tang, P.; Wu, R.; Wu, Q.; Zhang, C. The distinct roles of ROS in tumor immunity: from mechanisms to immunotherapeutic applications. *J. Hematol. Oncol.* **2026**, *19*, 16.

[34] Sun, X.; Zhou, X.; Shi, X.; Abed, O. A.; An, X.; Lei, Y. L.; Moon, J. J. Strategies for the development of metalloimmunotherapies. *Nat. Biomed. Eng.* **2024**, *8*, 1073-1091.

[35] Zhao, R.; Feng, L.; Zhu, Y.; Yu, C.; Zyuzin, M. V.; Gai, S.; Chen, D.; Zhang, S.; Zhu, H.; Yang, P. A Precision Mo4VC4-Based Nanomedicine for Effective Cancer Elimination by Harnessing Senescence Induction and Immunogenic Response. *Adv. Funct. Mater.* **2025**, *35*, 2420600.

[36] Wang, J.; Tian, Q.; Liu, Y.; Cai, C.-Y.; Fu, S.; Li, J.; Guan, Y.; Liao, X.; Su, D.; Sun, T. et al. Targeting metalloptosis in tumor therapy: from molecular mechanisms to application of metal nanoparticles. *Mol. Cancer* **2025**, *24*, 260.

[37] Cushing, B. L.; Kolesnichenko, V. L.; O'connor, C. J. Recent Advances in the Liquid-Phase Syntheses of Inorganic Nanoparticles. *Chem. Rev.* **2004**, *104*, 3893-3946.

[38] Linnane, E.; Haddad, S.; Melle, F.; Mei, Z.; Fairen-Jimenez, D. The uptake of metal–organic frameworks: a journey into the cell. *Chem. Soc. Rev.* **2022**, *51*, 6065-6086.

[39] Ma, Y.; Ma, Y.; Dreyer, S. L.; Wang, Q.; Wang, K.; Goonetilleke, D.; Omar, A.; Mikhailova, D.; Hahn, H.; Breitung, B. et al. High‐Entropy Metal‐Organic Frameworks for Highly Reversible Sodium Storage. *Adv. Mater.* **2021**, *33*, 2101342.

Just Accepted

[40] Wang, D.; Wu, H.; Phua, S. Z. F.; Yang, G.; Qi Lim, W.; Gu, L.; Qian, C.; Wang, H.; Guo, Z.; Chen, H. et al. Self-assembled single-atom nanozyme for enhanced photodynamic therapy treatment of tumor. *Nat. Commun.* **2020**, *11*, 357.

[41] Wang, D.; Wu, H.; Wang, C.; Gu, L.; Chen, H.; Jana, D.; Feng, L.; Liu, J.; Wang, X.; Xu, P. et al. Self‐Assembled Single‐Site Nanozyme for Tumor‐Specific Amplified Cascade Enzymatic Therapy. *Angew. Chem. Int. Ed.* **2021**, *60*, 3001-3007.

[42] Meng, X.; Fan, H.; Chen, L.; He, J.; Hong, C.; Xie, J.; Hou, Y.; Wang, K.; Gao, X.; Gao, L. et al. Ultrasmall metal alloy nanozymes mimicking neutrophil enzymatic cascades for tumor catalytic therapy. *Nat. Commun.* **2024**, *15*, 1626.

[43] Ma, B.; Wang, S.; Liu, F.; Zhang, S.; Duan, J.; Li, Z.; Kong, Y.; Sang, Y.; Liu, H.; Bu, W. et al. Self-Assembled Copper–Amino Acid Nanoparticles for in Situ Glutathione "AND" H2O2 Sequentially Triggered Chemodynamic Therapy. *J. Am. Chem. Soc.* **2018**, *141*, 849-857.

[44] Chen, Y.; He, P.; Jana, D.; Wang, D.; Wang, M.; Yu, P.; Zhu, W.; Zhao, Y. Glutathione‐Depleting Organic Metal Adjuvants for Effective NIR‐II Photothermal Immunotherapy. *Adv. Mater.* **2022**, *34*, 2201706.

[45] Zhang, M.; Song, X.; Qin, Y.; Peng, Y.; Zhang, S.; Feng, W.; Huang, H.; Chen, Y.; Zhou, J. Single-atom–doped piezocatalyst induces copper-free cuproptosis in tumor therapy. *Sci. Adv.* **2025**, *11*, eadt8451.

[46] Ji, S.; Jiang, B.; Hao, H.; Chen, Y.; Dong, J.; Mao, Y.; Zhang, Z.; Gao, R.; Chen, W.; Zhang, R. et al. Matching the kinetics of natural enzymes with a single-atom iron nanozyme. *Nat. Catal.* **2021**, *4*, 407-417.

[47] Dong, S.; Dong, Y.; Liu, B.; Liu, J.; Liu, S.; Zhao, Z.; Li, W.; Tian, B.; Zhao, R.; He, F. et al. Guiding Transition Metal‐Doped Hollow Cerium Tandem Nanozymes with Elaborately Regulated Multi‐Enzymatic Activities for Intensive Chemodynamic Therapy. *Adv. Mater.* **2022**, *34*, 2107054.

[48] Wei, S.; Ma, W.; Sun, M.; Xiang, P.; Tian, Z.; Mao, L.; Gao, L.; Li, Y. Atom-pair engineering of single-atom nanozyme for boosting peroxidase-like activity. *Nat. Commun.* **2024**, *15*, 6888.

[49] Liu, Y.; Zhao, H.; Niu, R.; Zhang, B.; Lim, B. T. G.; Song, S.; Wang, Y.; Zhang, H.; Zhao, Y. Single-site nanozyme with exposed unsaturated Cu-O2 sites for tumor therapy by coordinating innate immunity and vasculature normalization. *Chem* **2025**, *11*, 102297.

[50] Jiang, B.; Duan, D.; Gao, L.; Zhou, M.; Fan, K.; Tang, Y.; Xi, J.; Bi, Y.; Tong, Z.; Gao, G. F. et al. Standardized assays for determining the catalytic activity and kinetics of peroxidase-like nanozymes. *Nat. Protoc.* **2018**, *13*, 1506-1520.

[51] Dong, H.; Du, W.; Dong, J.; Che, R.; Kong, F.; Cheng, W.; Ma, M.; Gu, N.; Zhang, Y. Depletable peroxidase-like activity of Fe3O4 nanozymes accompanied with separate migration of electrons and iron ions. *Nat. Commun.* **2022**, *13*, 5365.

[52] Liu, Y.; Wang, J. Multivalent metal catalysts in Fenton/Fenton-like oxidation system: A critical review. *Chem. Eng. J.* **2023**, *466*, 143147.

[53] Hegner, F. S.; Galán-Mascarós, J. R.; López, N. Lowering the Water Oxidation Overpotential by Spin-Crossover in Cobalt Hexacyanoferrate. *The Journal of Physical Chemistry Letters* **2022**, *13*, 4104-4110.

[54] Cai, H.; He, S.; Yang, H.; Huang, Q.; Luo, F.; Hu, Q.; Zhang, X.; He, C. Highly Exposed Ultra‐Small High‐Entropy Sulfides with d‐p Orbital Hybridization for Efficient Oxygen Evolution. *Adv. Mater.* **2025**, *37*, 2508610.

[55] Tang, L.; Yang, X.; Yin, Q.; Cai, K.; Wang, H.; Chaudhury, I.; Yao, C.; Zhou, Q.; Kwon, M.; Hartman, J. A. et al. Investigating the optimal size of anticancer nanomedicine. *Proceedings of the National Academy of Sciences* **2014**, *111*, 15344-15349.

[56] Yang, Y.; Sun, B.; Zuo, S.; Li, X.; Zhou, S.; Li, L.; Luo, C.; Liu, H.; Cheng, M.; Wang, Y. et al. Trisulfide bond–mediated doxorubicin dimeric prodrug nanoassemblies with high drug loading, high self-assembly stability, and high tumor selectivity. *Sci. Adv.* **2020**, *6*, eabc1725.

[57] Abe, K.; Ikeda, M.; Ide, T.; Tadokoro, T.; Miyamoto, H. D.; Furusawa, S.; Tsutsui, Y.; Miyake, R.; Ishimaru, K.; Watanabe, M. et al. Doxorubicin causes ferroptosis and cardiotoxicity by intercalating into mitochondrial DNA and disrupting Alas1-dependent heme synthesis. *Sci. Signaling* **2022**, *15*, eabn8017.

[58] Thulasingam, M.; Orellana, L.; Nji, E.; Ahmad, S.; Rinaldo-Matthis, A.; Haeggström, J. Z. Crystal structures of human MGST2 reveal synchronized conformational changes regulating catalysis. *Nat. Commun.* **2021**, *12*, 1728.

[59] Li, Z.; Fu, J.; Li, N.; Shen, L. Quantitative proteome analysis identifies MAP2K6 as potential regulator of LIFR-induced radioresistance in nasopharyngeal carcinoma cells. *Biochem. Biophys. Res. Commun.* **2018**, *505*, 274-281.

[60] Chauvin, S. D.; Ando, S.; Holley, J. A.; Sugie, A.; Zhao, F. R.; Poddar, S.; Kato, R.; Miner, C. A.; Nitta, Y.; Krishnamurthy, S. R. et al. Inherited C-terminal TREX1 variants disrupt homology-directed repair to cause senescence

Just Accepted

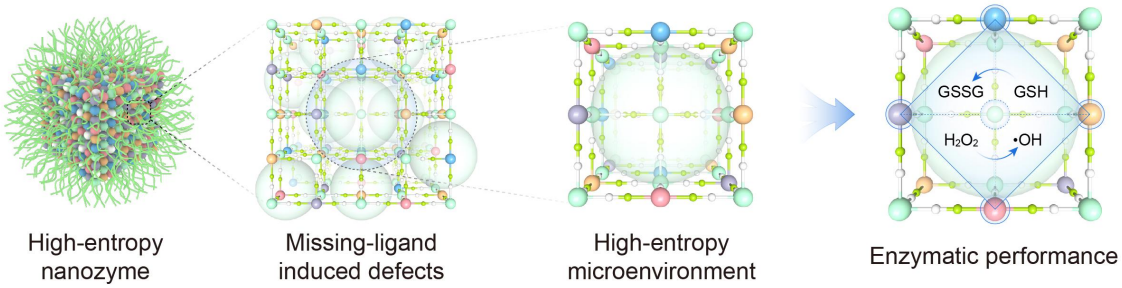
and DNA damage phenotypes in Drosophila, mice, and humans. *Nat. Commun.* **2024**, *15*, 4696.

[61] Lee, S. S.; Fu, N. Y.; Sukumaran, S. K.; Wan, K. F.; Wan, Q.; Yu, V. C. TRIM39 is a MOAP-1-binding protein that stabilizes MOAP-1 through inhibition of its poly-ubiquitination process. *Exp. Cell Res.* **2009**, *315*, 1313-1325.

[62] Smagris, E.; Gilyard, S.; Basuray, S.; Cohen, J. C.; Hobbs, H. H. Inactivation of Tm6sf2, a Gene Defective in Fatty Liver Disease, Impairs Lipidation but Not Secretion of Very Low Density Lipoproteins *. *J. Biol. Chem.* **2016**, *291*, 10659-10676.

Just Accepted

Entry for the Table of Contents



A ligand-deficient high-entropy Prussian blue nanozyme couples multimetal electronic disorder with catalytic redox activation. Coordinated glutathione exhaustion and hydroxyl radical generation enforce tumor-selective oxidative disequilibrium, driving both tumor destruction and immune microenvironment remodeling.

Just Accepted

Electronic Supporting Information

Entropy-regulated electronic structure of high-entropy Prussian blue analogues drives tumor-selective redox-immunotherapy

Chenyang Bi[1,2], Qingshan Liu[2,3], Xingyan Chen[1], Wei Cao[4], Lei Zhang[4], Hao Zhang[1], Jiahe Yang[1], Yafei Qu[1], Hongda Shi[1], Tao Wei*[2,3], Qianwang Chen[1], Evgeny Kataev*[3], and Dongdong Wang*[1,4]

1 Hefei National Research Center for Physical Sciences at the Microscale, Department of Materials Science and Engineering, University of Science and Technology of China, Hefei 230026, China
2 State Key Laboratory of Precision and Intelligent Chemistry, University of Science and Technology of China, Hefei 230026, P. R. China.
3 Department of Chemistry and Pharmacy, Friedrich Alexander University of Erlangen-Nurnberg, Erlangen 91058, Germany.
4 Department of Pharmacy, The First Affiliated Hospital of USTC, University of Science and Technology of China, Hefei 230001, China

✉Address correspondence to Dongdong Wang, wangdd13@ustc.edu.cn; Evgeny Kataev, evgeny.kataev@fau.de; Tao Wei, taowei2@ustc.edu.cn

Supporting information to https://doi.org/10.26599/NR.2026.94909182

Just Accepted

Table of Contents

1. Experimental procedures
    1.1 Cell lines and animals
    1.2 Calculation of configurational entropy
    1.3 Computational method
    1.4 Catalytic activity toward GSH
    1.5 Quantitative analysis of GSH depletion
    1.6 Michaelis-Menten curve of GSHOx-like activity measurement
    1.7 Detection of H_2O_2 generation during GSH consumption
    1.8 Valence state analysis of high-entropy species
    1.9 Catalytic activity toward H_2O_2
    1.10 POD-like activity measurement under various physiological conditions
    1.11 Hydroxyl radical detection
    1.12 Michaelis-Menten curves of POD-like activity measurement
    1.13 Endocytosis study
    1.14 In vitro cytotoxicity study
    1.15 Stability and degradation behavior of HENEs
    1.16 Intracellular GSH and ROS assay
    1.17 GSH content analysis in tumor tissues
    1.18 Live/dead staining assay
    1.19 In vitro apoptosis analysis
    1.20 Hemolysis and coagulation assays
    1.21 In vivo metabolic study of HENEs
    1.22 In vivo fluorescence imaging
    1.23 In vivo tumor treatment
    1.24 In vivo biocompatibility analysis
    1.25 Pathological investigation
    1.26 Transcriptomics analysis
    1.27 Western blot analysis
    1.28 Cell cycle analysis
    1.29 Analysis of tumor-infiltrating immune cells
    1.30 Statistical analysis
2. Supplementary tables and figures

Just Accepted

1. Experimental procedures

1.1 Cell lines and animals

Mouse mammary carcinoma 4T1 cells and human umbilical vein epithelial cells HUVECs were originally obtained from the American Type Culture Collection (ATCC). 4T1 cells were cultured in Roswell Park Memorial Institute 1640 medium (RPMI-1640) supplemented with fetal bovine serum (10%) and antibiotics (1%, penicillin/streptomycin). HUVECs were cultured in Dulbecco's modified Eagle's medium (DMEM) supplemented with fetal bovine serum (10%) and antibiotics (1%, penicillin/streptomycin). All cells were cultured in a humidified incubator containing 5% CO_2 at 37 °C. BALB/c female mice (5~7 weeks) were purchased from Hangzhou Ziyuan Experimental Animal Technology. All animal experiments were performed according to protocols approved by the Animal Care and Use Committee at the University of Science and Technology of China (approval number: 2022-N(A)-021). All research complied with all relevant ethical regulations: for the mice with a single tumor, the volume of the tumor (Volume = 0.5 × L × W^2, L is the length of tumor and W is the width of tumor), and the length should not exceed 20 mm. All the mice were grouped and housed under a 12 h light/dark cycle, 50~70% humidity, and at 18~22 °C ambient temperature.

1.2 Calculation of configurational entropy

For the prepared PBA-based nanozymes, the configurational entropy of M_a site per mole can be expressed as:

$$\Delta S_{conf} = -R \sum_{i=1}^{n} x_i \ln x_i \qquad \textbf{(Formula S1)}$$

where R is the gas constant, and x_i represents the mole fraction of each metal species in M_a sites of PBAs.

1.3 Computational method

Density functional theory calculations were performed using VASP with the PAW method. The GGA-PBE functional was employed for exchange-correlation interactions, and van der Waals interactions were treated using the DFT-D3 method. A 15 Å vacuum layer was applied. The plane-wave cutoff energy was set to 520 eV, and electronic convergence was achieved at 1×10^{-5} eV with Gaussian smearing (σ = 0.05 eV). All structures were fully optimized until the residual forces were below 0.03 eV $Å^{-1}$. Brillouin zone sampling was performed using a 1 × 1 × 1 Monkhorst-Pack k-point grid.

1.4 Catalytic activity toward GSH

Under ambient conditions, PBA-based nanozymes (LENEs, MENEs-Cu, and HENEs, 1 mg/mL) and GSH (1 mM) were mixed evenly. After standing for 6 h, the supernatant (500 μL) was collected by centrifugation and added to the 5,5'-Dithiobis-(2-nitrobenzoic acid) (DTNB) working solution (100 μL, 0.25 mg/mL). After 5 min incubation, the UV-vis absorption spectra within the 360-500 nm band were measured to verify the catalytic effect of PBA-based nanozymes toward GSH.

1.5 Quantitative analysis of GSH depletion

To verify the GSH depletion ability of HENEs, a high-concentration GSH solution (10 mM) was mixed with HENEs (1 mg/mL). At predetermined time points, 1 mL of the solution was collected and centrifuged to obtain the supernatant. A portion of the supernatant was used for proton

Just Accepted

nuclear magnetic resonance (^{1}H NMR) spectroscopy. For NMR analysis, 500 μL of the supernatant was mixed with 10 μL of maleic acid (10 mM) and 50 μL of deuterated water in an NMR tube. Another portion of the supernatant was used to determine the GSH content at predetermined time points. The absorbance of the supernatant at 412 nm was measured by the GSH detection kit (Beyotime), and the relative GSH/GSSG ratio was calculated based on the GSH standard curve generated by the DTNB colorimetric method.

1.6 Michaelis-Menten curve of GSHOx-like activity measurement

HENEs (250 μg/mL) were mixed with GSH solutions of various concentrations (0.05, 0.1, 0.2, 0.5, 0.6, 0.8, and 1 mM), and the absorbance at 412 nm was measured after the addition of the DTNB working solution. The GSH content and initial degradation rate were calculated based on the absorbance values using a GSH standard curve. The Michaelis-Menten curve was plotted to determine the maximum reaction rate (V_{max}) and Michaelis constant (K_m).

1.7 Detection of H_2O_2 generation during GSH consumption

An H_2O_2 standard curve was established in a 96-well plate by mixing 100 μL titanium sulfate solution (0.16 g titanium sulfate, 4.165 mL sulfuric acid, 20.835 mL water) with 50 μL water and 50 μL H_2O_2 (0.5, 1, 4 mM) and measuring the absorbance at 405 nm to obtain a linear calibration. For H_2O_2 detection, 100 μL titanium sulfate solution was mixed with 50 μL GSH (20 mM) and 50 μL HENEs (2 mg/mL). Absorbance at 405 nm was recorded every 5 min and H_2O_2 concentrations were calculated using the standard curve.

1.8 Valence state analysis of high-entropy species

To explore the source of GSHOx-like activity of HENEs, HENEs were incubated with GSH for 24 h. Thereafter, the resulting precipitate (termed as HENEs-G) was collected by centrifugation and characterized by X-ray photoelectron spectroscopy.

1.9 Catalytic activity toward H_2O_2

To compare the Fenton-like catalytic ability of PBA-based nanozymes with various entropy values, PBA-based nanozymes (LENEs, MENEs-Cu, and HENEs, 100 μg/mL), H_2O_2 (10 mM), and TMB (5 mM) were mixed evenly in a NaAc-HAc buffer (pH 5.0). The absorbance change at 652 nm of the solution was measured every 10 s for a total duration of 360 s.

1.10 POD-like activity measurement under various physiological conditions

The ability of PBA-based nanozymes (LENEs, MENEs-Cu, and HENEs) to oxidize TMB under various pH conditions was fully investigated. The reaction was conducted in a NaAc-HAc buffer with various pH values (5.0, 6.5, and 7.4). The initial reaction rate was calculated based on the absorbance change at 652 nm over the first 30 s of the reaction. For the POD-like specific activity assay, samples were dispersed in a NaAc-HAc buffer (pH 5.0) at 12, 9, 6, and 3 ppm (100 μL), then mixed with 50 μL TMB (20 mM) and 50 μL H_2O_2 (8 M). The absorbance at 652 nm, corresponding to TMB oxidation, was recorded every 10 s. The absorbance increase over time was plotted, enzyme activity units were calculated using the standard formula, and specific activity was determined.

Just Accepted

1.11 Hydroxyl radical detection

PBA-based nanozymes (LENEs, MENEs-Cu, and HENEs, 100 μg/mL) and 5,5-dimethyl-1-pyrroline N-oxide (DMPO, 100 mM) were mixed in a NaAc-HAc buffer (pH 5.0). After adding H_2O_2 (10 mM) and ultrasonicating the solution for 30 s, it was immediately transferred to a quartz tube for ESR analysis. Additionally, terephthalic acid was used as a specific binding agent for •OH. PBA-based nanozymes (LENEs, MENEs-Cu, and HENEs, 100 μg/mL), H_2O_2 (10 mM), and terephthalic acid (5 mM) were mixed in NaAc-HAc buffer (pH 5.0), and the fluorescence intensity at 432 nm (excitation wavelength at 320 nm) was measured after 5 min.

1.12 Michaelis-Menten curves of POD-like activity measurement

The POD-like activity reaction kinetics and cascade enzymatic activities of HENEs were further studied. HENEs or HENEs-G (100 μg/mL) were mixed with TMB (5 mM) in NaAc-HAc buffer (pH 5.0), and H_2O_2 solution of various final concentrations (100, 250, 500, 750, 1000, 1500, and 2000 mM) was added. The absorbance at 652 nm was measured every 10 s for a total of 60 s. The initial reaction rate was calculated based on the absorbance-time curve, and the Michaelis-Menten curve was fitted to determine the maximum reaction rate (V_{max}) and Michaelis constant (K_m).

1.13 Endocytosis study

HENEs (1 mg/mL) and Cy5.5-PEG-SH (1 mg/mL) were mixed and stirred for 24 h for efficient conjugation of Cy5.5. The resulting product HENEs-Cy5.5 was centrifuged and redispersed in the culture medium. 4T1 cells were seeded in 12-well plates with coverslips at the bottom at 1.0×10^5 cells per well and left to adhere for 12 h at 37 °C with 5% CO_2. The culture medium was then replaced with a fresh one containing HENEs-Cy5.5 (200 μg/mL), and lysosome and cell nuclei staining were performed with Lyso-Tracker Green (Beyotime) and Hoechst 33342 (Abcam) at predetermined time points (0, 1, 2, and 4 h). The staining procedures followed the fluorescent probe instructions, and then the cells were imaged under a confocal laser scanning microscopy (CLSM, Zeiss LSM 980).

1.14 In vitro cytotoxicity study

Both 4T1 and HUVECs were seeded in 96-well plates at a seeding density of 1.0×10^4 cells per well and incubated at 37 °C with 5% CO_2 for 12 h. Once the cell density reached 60%, the cells were co-cultured with PBA-based nanozymes (LENEs, MENEs-Cu, and HENEs) at various concentrations (0, 25, 50, 100, and 200 ppm) for another 24 or 48 h. The relative cell viability was then assessed using a standard MTT assay.

1.15 Stability and degradation behavior of HENEs

HENEs were dispersed in pH 7.4 or 5.0 buffer containing 10 mM GSH, and the samples were collected at different time points for TEM analysis.

1.16 Intracellular GSH and ROS assay

4T1 cells (1.0×10^5 cells per well) were seeded in glass-bottomed culture dishes for 12 h. Thereafter, the cells were treated with different PBA-based nanozymes (LENEs, MENEs-Cu, and

Just Accepted

HENEs) at a concentration of 200 ppm for another 12 h. The redox balance of the cells was determined using assay kits. The level of intracellular reducing substance GSH was elevated using a ThiolTracker Violet reagent (Invitrogen). The intracellular ROS level was detected using a ROS assay kit 2',7'-dichlorodihydrofluorescein diacetate (DCFH-DA, Beyotime). The intracellular hydroxyl radical generation was detected using Hydroxyphenyl Fluorescein (MCE). After incubation with the assay kit for 30 min, the cell nuclei were further stained with Hoechst 33342 for 10 min. Before observing under a fluorescence microscope (IX73, Olympus), the cells were gently rinsed three times with phosphate-buffered saline (PBS) to remove unbound dye.

1.17 GSH content analysis in tumor tissues

For tumor tissues, 4T1 tumor-bearing mice were randomly divided into two groups (n = 3). The dosing group was administrated with HENEs (10 mg/kg) via tail vein injection, and the control group received PBS. On the 14th day after the initiation of treatment, the mice were euthanized, and tumor tissues were collected. The homogenates were prepared from tumor tissues of control and HENEs-treated groups, and the supernatant was collected. GSH levels in tumor tissues were measured using a GSH detection kit (Beyotime).

1.18 Live/dead staining assay

4T1 cells (1.0×10^5 cells per well) were seeded in glass-bottomed culture dishes and incubated for 12 h. Once the cell density reached 60%, the original culture medium was replaced with a fresh one containing PBA-based nanozymes (LENEs, MENEs-Cu, and HENEs) at a concentration of 200 ppm and co-cultured for another 24 h. The live and dead cells were stained with calcein-AM (Invitrogen) and propidium iodide (PI, Invitrogen), respectively. The cells were co-incubated with the fluorescent probes for 15 min, followed by the removal of the unbound dye with PBS. The cells were then observed under a fluorescence microscope.

1.19 In vitro apoptosis analysis

4T1 cells were seeded in 12-well plates at a density of 1.0×10^5 cells per well and cultured for 12 h at 37 °C with 5% CO_2. Once the cell density reached 60%, 4T1 cells were treated with PBA-based nanozymes (LENEs, MENEs-Cu, and HENEs) at a concentration of 200 ppm for 24 h. The cells from the indicated groups were collected and stained using an annexin V-FITC/PI apoptosis detection kit (Beyotime) according to the protocol provided by the manufacturer. The stained cells were dispersed into PBS and quantitatively analyzed using flow cytometry (CytoFLEX LX, Beckman Coulter).

1.20 Hemolysis and coagulation assays

Blood was collected from healthy BALB/c mice into anticoagulation tubes and centrifuged to isolate red blood cells, which were then suspended in PBS. Equal amounts of red blood cells were treated with HENEs at indicated concentrations (0, 25, 50, 100, 200, 400, and 800 ppm). The deionized water served as the positive control. After incubation at 37 °C for 3 h, the mixture was centrifuged, and the absorbance of the supernatant at 540 nm was measured. The hemolysis rate was calculated using PBS as the negative control. For the coagulation assay, fresh blood from mice was collected into EP tubes and immediately treated with HENEs at indicated concentrations (0, 25, 50, 100, 200, 400, and 800 ppm). After incubation for 90 s, deionized

Just Accepted

water was added to the above EP tubes. The solution was centrifuged again to obtain the supernatant, and the absorbance of the supernatant at 540 nm was measured. The blood coagulation index was calculated using PBS as a negative control.

1.21 In vivo metabolic study of HENEs

Mice received a tail-vein injection of 100 μL of 2 mg/mL HENEs. Blood and major organs were collected at 1, 2, and 7 days post-injection, digested in aqua regia, and the metal ion concentrations in the resulting solutions were measured by ICP-AES. The HENEs concentrations were then calculated according to their chemical composition.

1.22 In vivo fluorescence imaging

In vivo fluorescence imaging was conducted using Cy5.5 as a fluorescent agent in 4T1 tumor-bearing female mice. Firstly, HENEs (2 mg/mL) and Cy5.5-PEG-SH (1.5 mg/mL) were mixed evenly in PBS and stirred for 24 h for efficient conjugation of Cy5.5. When the tumor size reached about 60 mm^3, 100 μL of free Cy5.5-COOH (control group) and HENEs-Cy5.5 (equivalent dose based on Cy5.5: 2.5 mg/kg) solution was intravenously administrated. Whole-body fluorescence imaging (excitation wavelength: 675 nm, emission wavelength: 720 nm) was conducted using an in vivo imaging system (IVIS spectrum, PerkinElmer) at predetermined time points. At the endpoint of the treatment, the mice were euthanized, and the heart, liver, spleen, lung, kidney, and tumor tissue were dissected for ex vivo fluorescence imaging. Data analysis was conducted using the Living Image software (version 4.7.4, PerkinElmer).

1.23 In vivo tumor treatment

Balb/c mice (female, 6-8 weeks old) were subcutaneously inoculated with 2.0×10^6 4T1 cells per mouse into the right flank. When the average tumor volume reached 60 mm^3, the 4T1 tumor-bearing mice were randomly divided into 5 groups (n = 5), including the control group (PBS), DOX group, LENEs group, MENEs-Cu group, and HENEs group. Mice from different groups were intravenously administrated with 100 μL of PBS, DOX (5 mg/kg), LENEs (10 mg/kg), MENEs-Cu (10 mg/kg), and HENEs (10 mg/kg) on days 0, 1, and 2. The tumor volume and body weight of mice were monitored daily, and the relative tumor volume (V/V_0) was calculated with the tumor volume on day 0 as the initial size before drug administration. At the end of the treatments, all mice were euthanized, and the tumor tissues were excised and weighed. Additionally, the heart, liver, spleen, lung, kidney, and intestine were harvested and preserved in paraformaldehyde for further analysis.

1.24 In vivo biocompatibility analysis

In vivo biocompatibility analysis was conducted using healthy Balb/c female mice. Typically, the mice (n = 3) were intravenously administrated with PBS or HENEs (10 mg/kg). The blood samples were collected from the mice on day 2 and day 14 post-administration. One portion of the blood was used for routine blood analysis, and indicators including red blood cell distribution width (RDW), platelets (PLT), mean corpuscular hemoglobin concentration (MCHC), mean corpuscular hemoglobin (MCH), mean corpuscular volume (MCV), hematocrit (HCT), hemoglobin (HGB), red blood cells (RBC), and white blood cells (WBC) were measured. Another portion of the blood was used for biochemical analysis. The liver and kidney function indicators

Just Accepted

including creatinine (Crea), urea nitrogen (BUN), alkaline phosphatase (ALP), aspartate aminotransferase (ALT), and alanine aminotransferase (AST) were measured. After the in vivo tumor treatment, the main organs of the mice were fixed with paraformaldehyde. After paraffin embedding and sectioning, histological analysis was performed using hematoxylin and eosin (H&E) staining.

1.25 Pathological investigation

After in vivo treatment, tumor tissues from different treatment groups were fixed with paraformaldehyde. The samples were subsequently embedded in paraffin and sectioned. H&E staining, terminal deoxynucleotidyl transferase-mediated dUTP-biotin nick end labeling (TUNEL) staining (ebiogo), ROS staining (ebiogo) and Ki-67 immunohistochemical staining (Anti-Ki67 Rabbit mAb, Abcam, Ab16667, dilution 1:200 and HRP-conjugated Goat Anti-Rabbit IgG with TSA fluorescent dye, Zhongkang, D1002plus-02RM, dilution 1:200) were performed by Zhongkang Biotech to assess tissue morphology, cell apoptosis, and tumor cell proliferation, respectively.

1.26 Transcriptomics analysis

4T1 tumor-bearing mice were randomly divided into two groups (n = 3). The dosing group was administrated with HENEs (10 mg/kg) via tail vein injection, and the control group received PBS. On the 14th day after the initiation of treatment, the mice were euthanized, and tumor tissues were collected. High-throughput sequencing and data analysis were conducted by Qingke Biotech to investigate the gene expression profile and treatment-related changes.

1.27 Western blot analysis

4T1 cells were seeded in 6-well plates at a density of 2.0×10^5 cells per well and cultured for 12 h at 37 °C with 5% CO_2. Once the cell density reached 60%, 4T1 cells were treated with HENEs. After co-incubation with HENEs for 12 h, cells were collected and lysed. Protein extracts were prepared and subjected to Western blot analysis to evaluate the expression levels of target proteins (GPX4 Polyclonal antibody, proteintech, 30388-1-AP, dilution 1:1000, GSR Recombinant monoclonal antibody, proteintech, 84480-2-RR, dilution 1:5000, goat-anti-rabbit IgG conjugated with HRP, proteintech, SA00001-2, dilution 1:10000).

1.28 Cell cycle analysis

4T1 cells were seeded in 6-well plates at a density of 2.0×10^5 cells per well and cultured for 12 h at 37 °C with 5% CO_2. Once the cell density reached 60%, 4T1 cells were treated with HENEs. After co-incubation with HENEs for 12 h, cells were collected and stained using the Cell Cycle and Apoptosis Detection Kit (Beyotime), followed by flow cytometry analysis.

1.29 Analysis of tumor-infiltrating immune cells

4T1 tumor-bearing mice were randomly divided into two groups (n = 3). The dosing group was administrated with HENEs (10 mg/kg) via tail vein injection, and the control group received PBS. On the 7th day after the initiation of treatment, the mice were euthanized, and tumor tissues were collected. Immune cells were isolated from tumor tissues for flow cytometry analysis (TruStain FcX™ anti-mouse CD16/32 antibody, Biolegend, 101319, dilution 1:500, Zombie

Just Accepted

Violet™ Fixable Viability Kit, Biolegend, 423113, dilution 1:5000, APC/Cyanine7 anti-mouse CD45 recombinant antibody, Biolegend, 157617, dilution 1:500, FITC anti-mouse CD3 antibody, Biolegend, 100203, dilution 1:500, PE anti-mouse CD4 antibody, Biolegend, 100407, dilution 1:500, APC anti-mouse CD8a antibody, Biolegend, 100711, dilution 1:500, AF647-conjugated anti-Foxp3 antibody, Biolegend, 126407, dilution 1:500, APC anti-mouse CD11c antibody, Biolegend, 117309, dilution 1:500, FITC anti-mouse CD80 antibody, Biolegend, 104705, dilution 1:500, PE anti-mouse CD86 antibody, Biolegend, 105007, dilution 1:500, PE anti-mouse/human CD11b antibody, Biolegend, 101207, dilution 1:500, AF488-conjugated anti-mouse F4/80 antibody, Biolegend, 123119, dilution 1:500, PE/Cyanine7 anti-mouse CD206 antibody, Biolegend, 141719, dilution 1:500, BV605-conjugated anti-mouse Gr-1 antibody, Biolegend, 108439, dilution 1:500).

1.30 Statistical analysis

All data were expressed as mean ± standard error of the mean (s.e.m.). The statistical analysis was conducted by One-way ANOVA. The value of p with 0.05 was established as the significance threshold. Asterisk (*) demarcates statistically significant differences in intergroup comparisons (*$p < 0.05$, **$p < 0.01$, ***$p < 0.001$), and the analysis was conducted using GraphPad Prism 8.0.

Just Accepted

2. Supplementary tables and figures

	Mn	Fe	Co	Cu	Zn	ΔS
HENEs	0.21	0.26	0.14	0.22	0.17	**1.59R**
	$Mn_{0.21}Fe_{0.26}Co_{0.14}Cu_{0.22}Zn_{0.17}[Co(CN)_6]_{0.67}$ 0.33					
MENEs-Mn	0	0.50	0.09	0.14	0.27	**1.19R**
	$Fe_{0.50}Co_{0.09}Cu_{0.14}Zn_{0.27}[Co(CN)_6]_{0.67}$ 0.33					
MENEs-Fe	0.18	0	0.21	0.45	0.16	**1.29R**
	$Mn_{0.18}Co_{0.21}Cu_{0.45}Zn_{0.16}[Co(CN)_6]_{0.67}$ 0.33					
MENEs-Co	0.24	0.45	0	0.08	0.23	**1.24R**
	$Mn_{0.24}Fe_{0.45}Cu_{0.08}Zn_{0.23}[Co(CN)_6]_{0.67}$ 0.33					
MENEs-Cu	0.26	0.45	0.09	0	0.20	**1.25R**
	$Mn_{0.26}Fe_{0.45}Co_{0.09}Zn_{0.20}[Co(CN)_6]_{0.67}$ 0.33					
MENEs-Zn	0.30	0.34	0.18	0.18	0	**1.35R**
	$Mn_{0.30}Fe_{0.34}Co_{0.18}Cu_{0.18}[Co(CN)_6]_{0.67}$ 0.33					
LENEs	0	0	1	0	0	**0R**
	$Co[Co(CN)_6]_{0.67}$ 0.33					

Table S1. The contents of transition metal species (Mn, Fe, Co, Cu, and Zn) of M_a sites in the prepared PBA-based nanozymes (determined by ICP-AES) with the corresponding chemical formulas and configuration entropies. The entropy value of HENEs was as high as 1.59R, according to the definition of high-entropy (HE). The entropy values of the five MENEs were all between 1.0R and 1.5R, belonging to medium-entropy (ME). LENEs had an entropy of 0R, belonging to low-entropy (LE).

Just Accepted

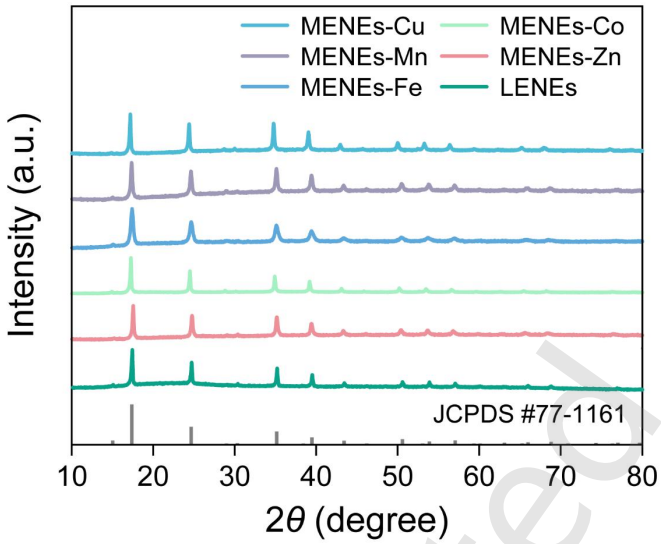


Figure S1. PXRD patterns of the prepared PBA-based nanozymes. The reference JCPDS#77-1161 corresponds to the crystal structure of the Prussian blue analog $Co_3[Co(CN)_6]_2$ ($[Co(CN)_6]_{2/3}$ $_{1/3}$, where represents the intrinsic one-third missing $[Co(CN)_6]$ ligands).

Just Accepted

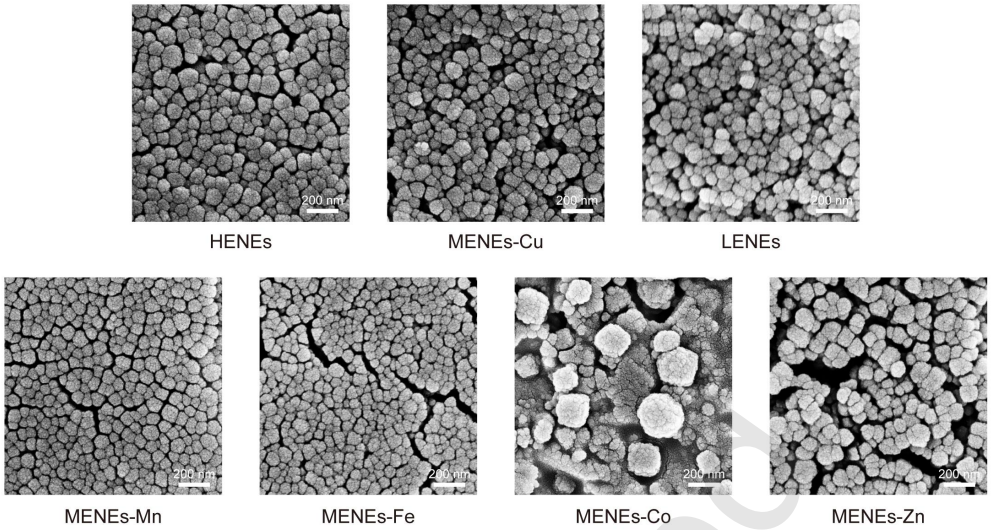


Figure S2. SEM images of the prepared PBA-based nanozymes (LENEs, MENEs, and HENEs). Except for MENEs-Co, the particle sizes of other PBA-based nanoenzymes were between 50~100 nm. Co-species was important for the synthesis of PBA-based nanozymes with small size.

Just Accepted

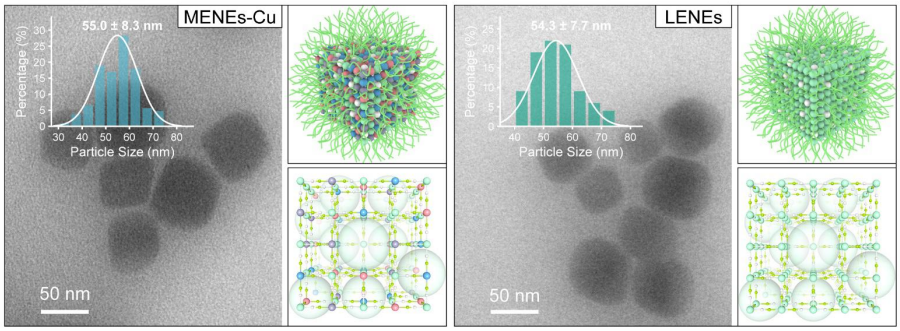


Figure S3. TEM images of MENEs-Cu and LENEs, along with statistical analysis of the average particle size from one hundred nanoparticles. The illustration shows the surface microenvironment and crystal structures of MENEs-Cu and LENEs.

Just Accepted

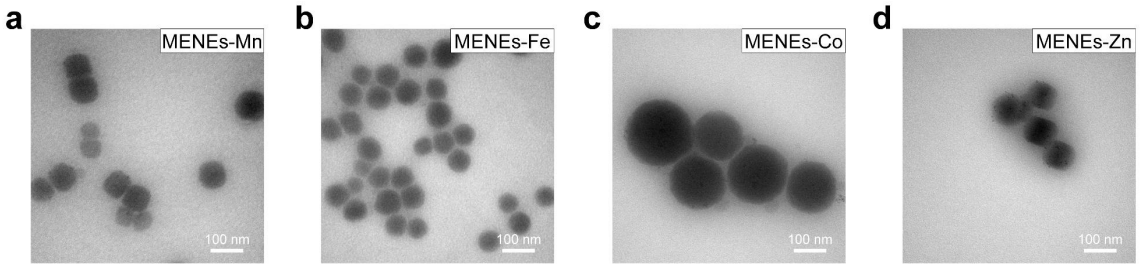


Figure S4. TEM images of MENEs-Mn (a), MENEs-Fe (b), MENEs-Co (c), and MENEs-Zn (d). The analysis results were consistent with the SEM characterization.

Just Accepted

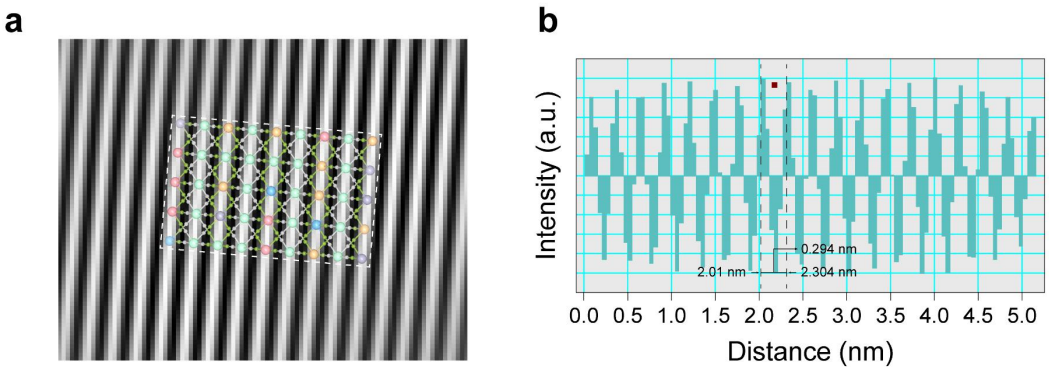


Figure S5. a) Interplanar distance of (222) crystal planes of HENEs. **b)** Analysis of interplanar distance of (222) crystal planes with inverse fast Fourier transform.

Just Accepted

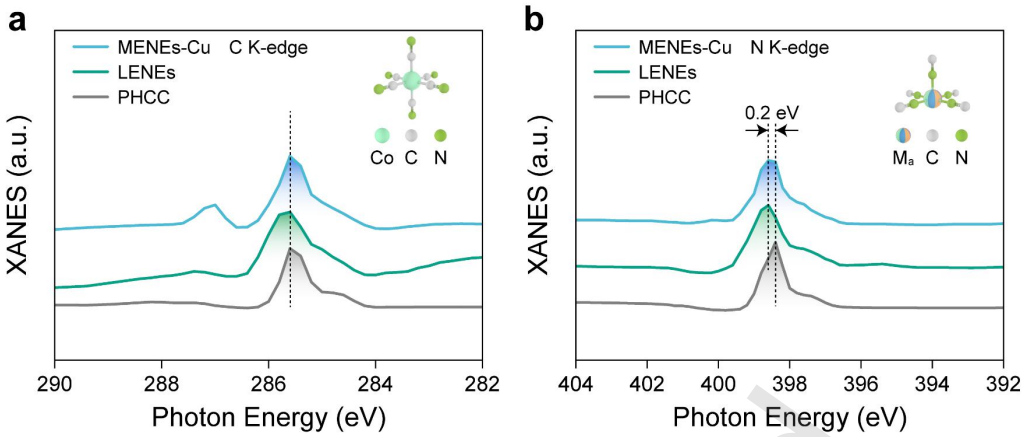


Figure S6. a) C K-edge NEXAFS spectra of LENEs and MENEs-Cu, with the structure model of the bridging ligand shown in the inset. **b)** N K-edge NEXAFS spectra of LENEs and MENEs-Cu, and the coordination structure of different species.

Just Accepted

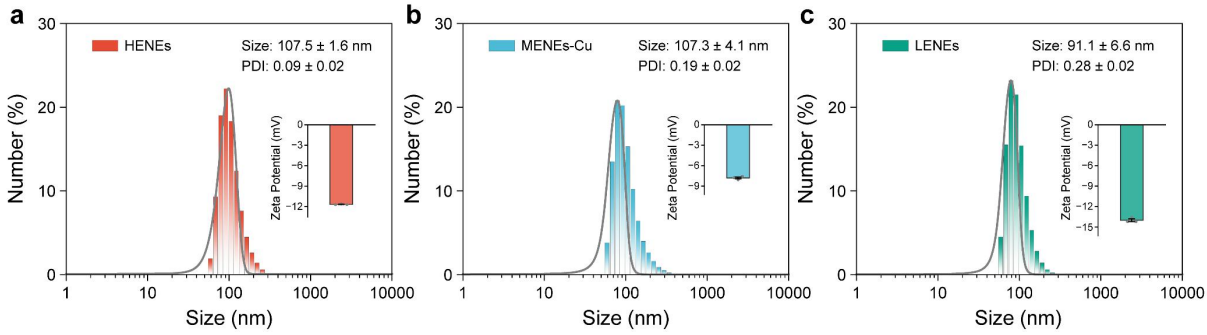


Figure S7. Hydrodynamic sizes of HENEs (a), MENEs-Cu (b) and LENEs (c) suspended in the aqueous solution. The inset shows the Zeta potential. Data are represented as mean ± s.e.m. from three independent experiments (n = 3).

Just Accepted

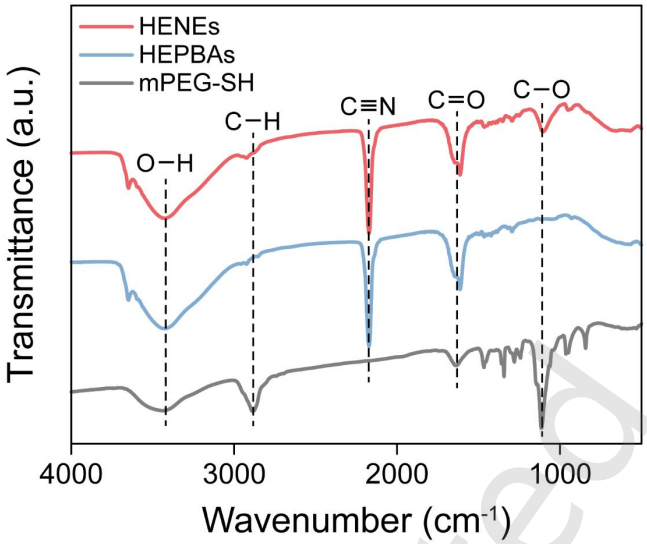


Figure S8. FT-IR spectra of HENEs, HEPBAs, and mPEG-SH.

Just Accepted

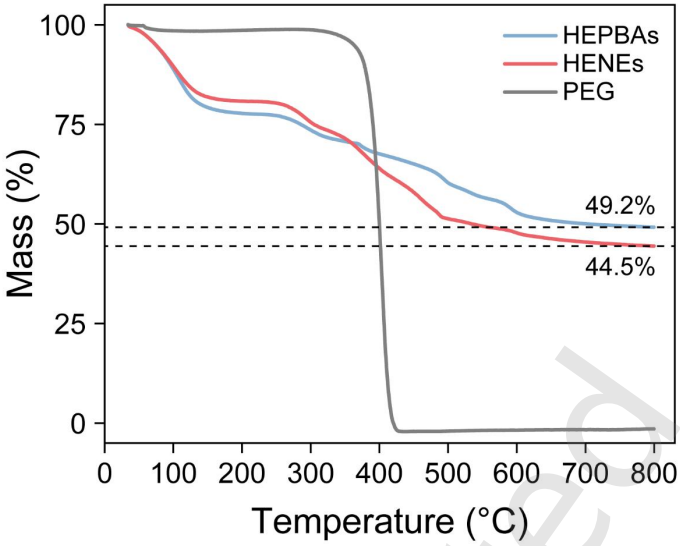


Figure S9. TGA of HENEs, HEPBAs, and PEG.

Just Accepted

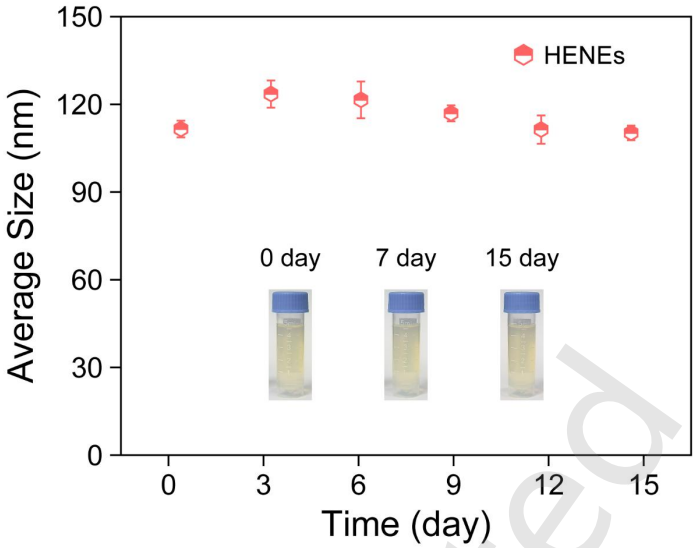


Figure S10. The hydrodynamic size of HENEs suspended in the aqueous solution within 15 days. Data are represented as mean ± s.e.m. from three independent experiments (n = 3).

Just Accepted

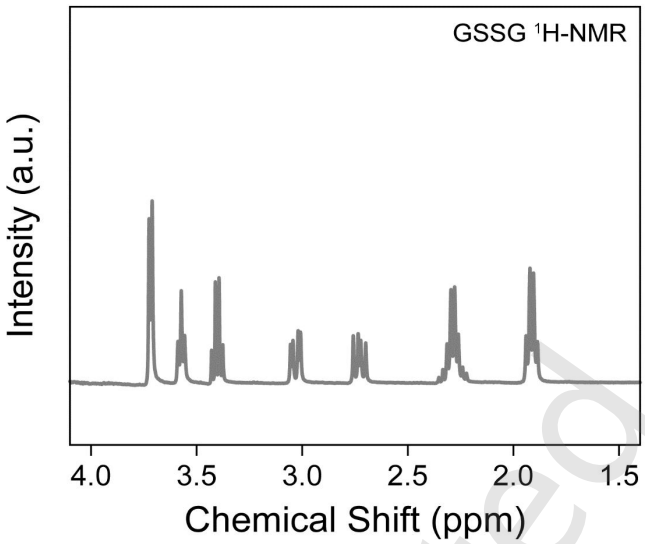


Figure S11. ^{1}H NMR spectrum of commercially available GSSG on the market.

Just Accepted

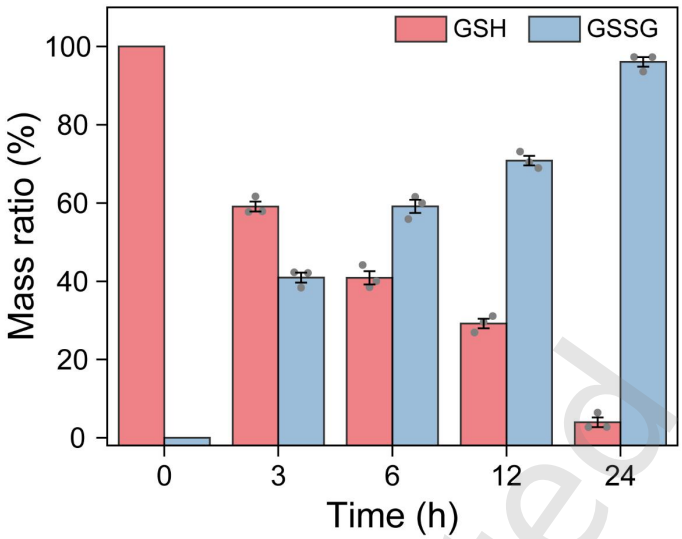


Figure S12. GSH and GSSG contents during the transformation process. Data are represented as mean ± s.e.m. from three independent experiments (n = 3).

Just Accepted

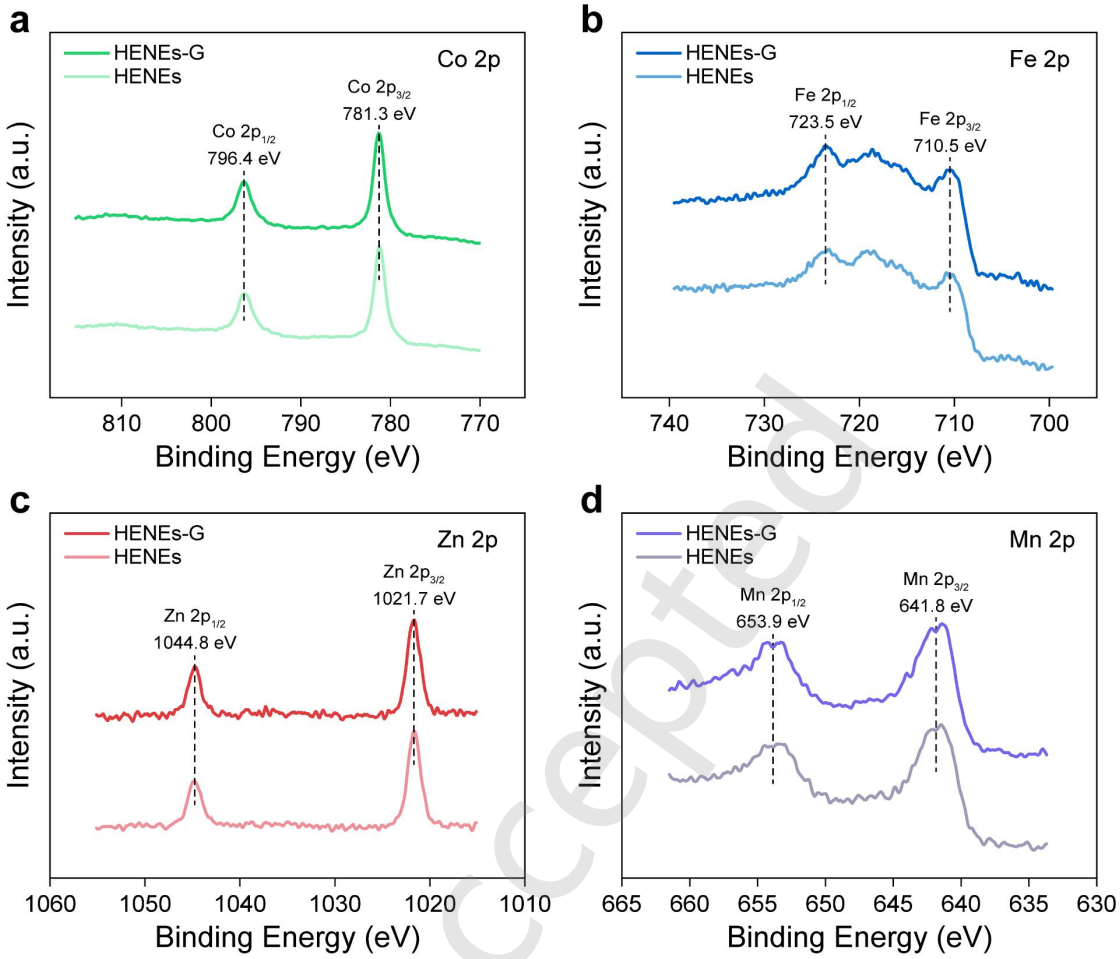


Figure S13. XPS analysis of Co (a), Fe (b), Zn (c) and Mn (d) species in HENEs and HENEs-G.

Just Accepted

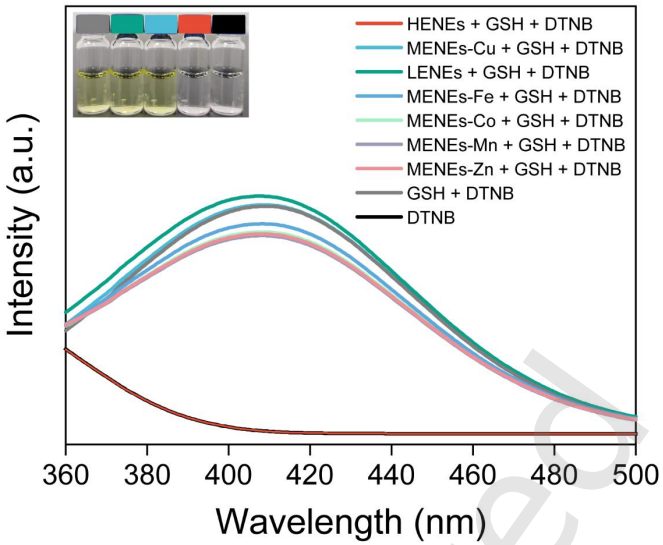


Figure S14. DTNB-based colorimetric reaction with PBA-based nanozymes.

Just Accepted

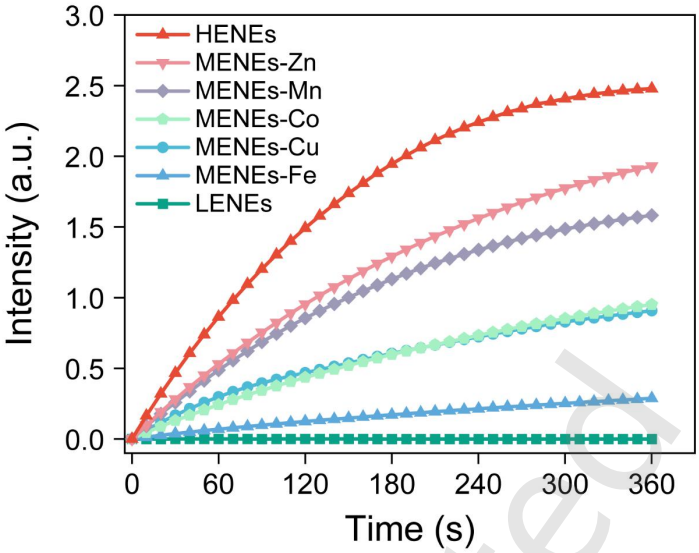


Figure S15. TMB-based colorimetric reaction with PBA-based nanozymes in the presence of H_2O_2 in NaAc-HAc buffer (pH 5.0).

Just Accepted

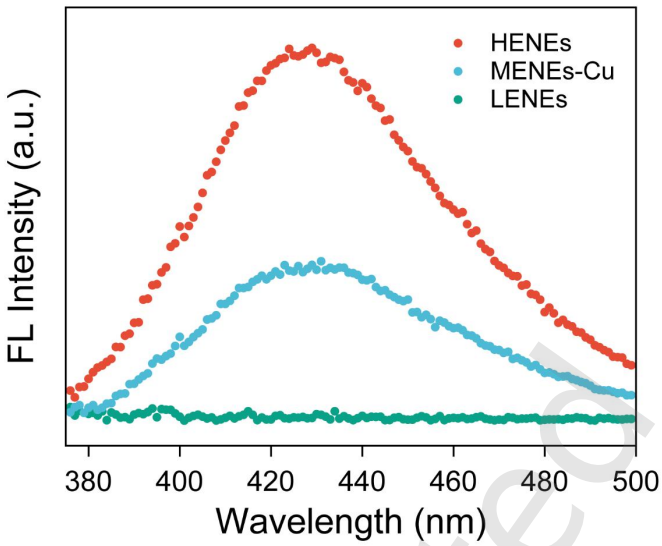


Figure S16. The fluorescence emission spectra for the specific determination of •OH radicals using TA.

Just Accepted

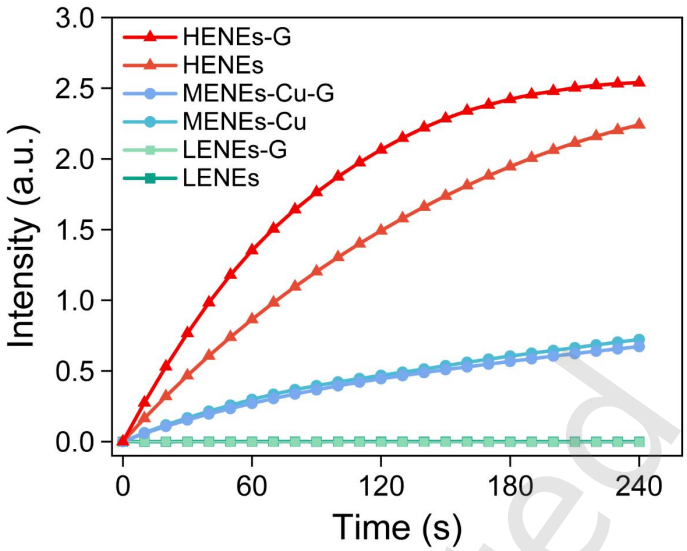


Figure S17. TMB-based colorimetric reaction with PBA-based nanozymes and PBA-based nanozymes-G in the presence of H_2O_2 in NaAc-HAc buffer (pH 5.0). The suffix G refers to the nanoenzymes that have been treated with GSH.

Just Accepted

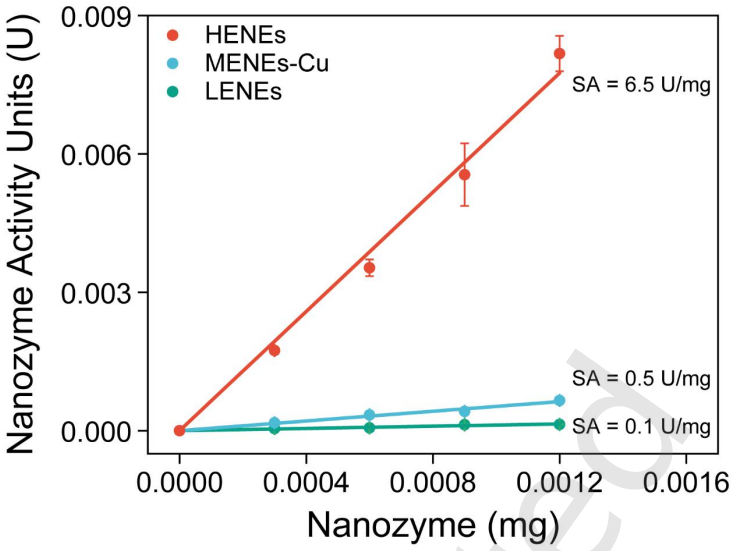


Figure S18. Specific activity analysis of LENEs, MENEs-Cu, and HENEs under the conditions at a pH value of 5.0 and 2 M hydrogen peroxide.

Just Accepted

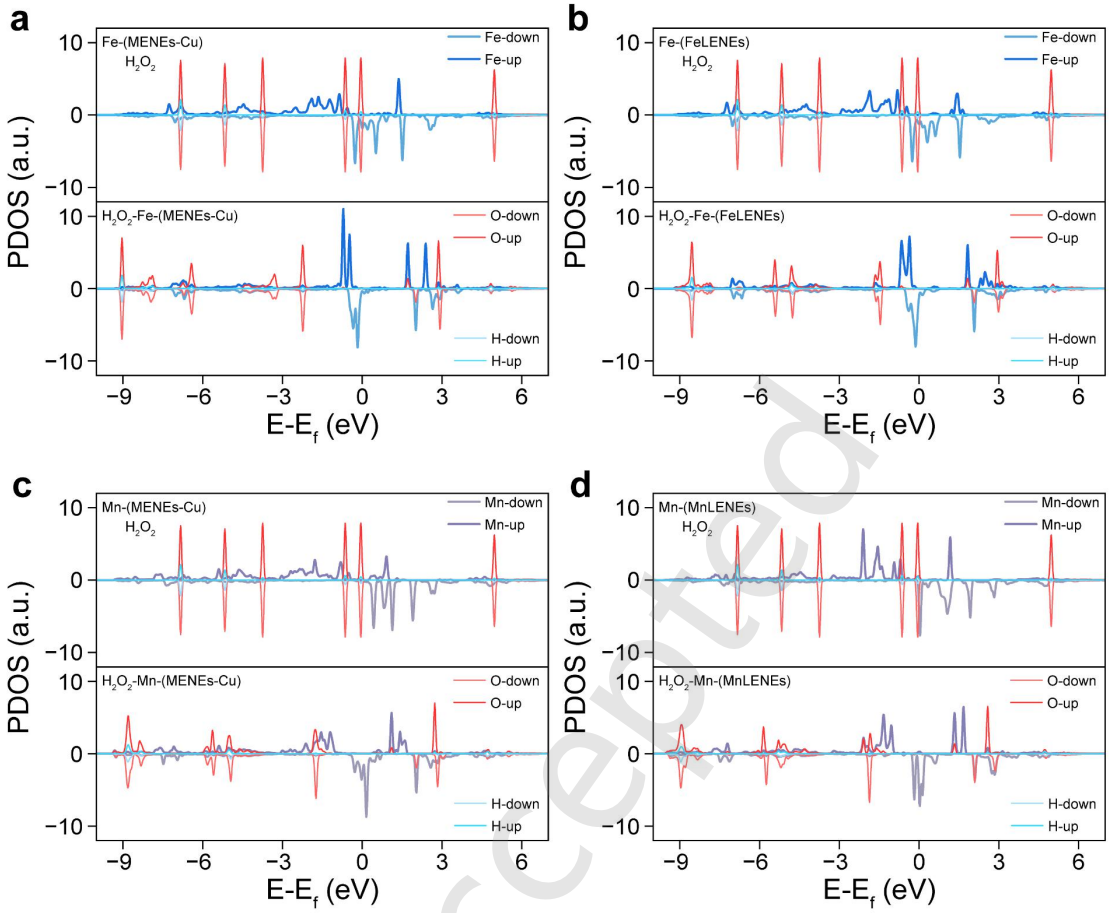


Figure S19. **a-d)** PDOS before and after H_2O_2 binding to Fe-N_5 and Mn-N_5 catalytic sites of MENEs-Cu and LENEs.

Just Accepted

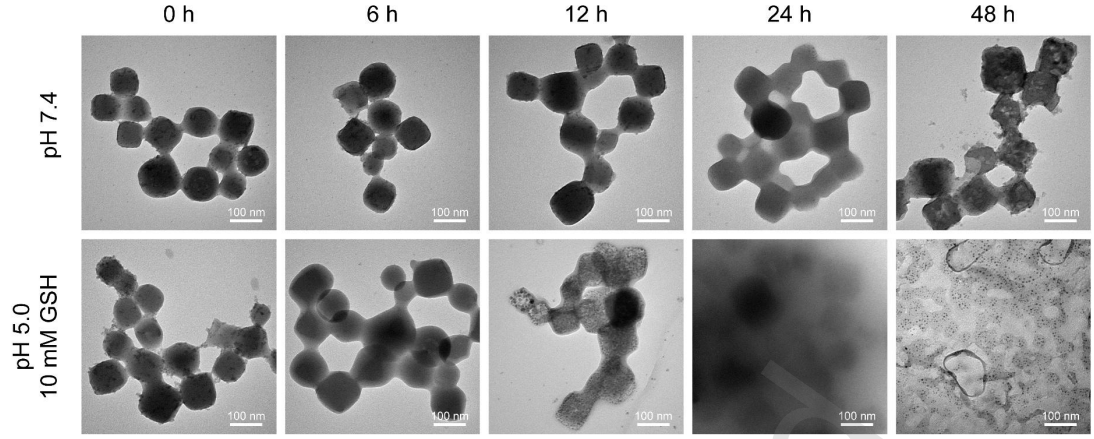


Figure S20. TEM images of HENEs under acidic conditions mimicking the normal physiological environment (pH~7.4) and lysosomal environment (pH~5.0) with 10 mM GSH within 48 h.

Given the acidic and GSH-rich environment of lysosomes, HENEs undergo partial framework degradation under lysosome-mimicking conditions (pH 5.0, 10 mM GSH), which may facilitate the release of constituent metal ions. These released Mn, Fe, Co, Cu, and Zn species could potentially participate in conventional metal-mediated redox reactions and contribute to intracellular ROS generation. Thus, metal-ion-mediated oxidative effects may represent an auxiliary component of the overall therapeutic activity of HENEs. Nevertheless, such ion-mediated effects alone are unlikely to fully account for the enhanced catalytic and cytotoxic performance of HENEs. The major catalytic function of HENEs originates from the high-entropy-regulated heterogeneous metal environment, in which multiple metal centers establish diverse coordination and electronic configurations and collectively facilitate redox reactions. In particular, Fe- and Mn-associated sites favor H_2O_2 activation and •OH generation, while the multimetallic environment supports GSHOx-like GSH consumption and H_2O_2 production. Consequently, HENEs establish a coupled redox cascade in which catalytic GSH depletion and H_2O_2 generation continuously feed peroxide-dependent •OH production. The substantially enhanced activity of HENEs compared with lower-and medium-entropy counterparts containing related metal species further suggests that the therapeutic effect cannot be simply ascribed to the presence or release of individual metal ions. Therefore, lysosomal degradation and subsequent metal-ion release are considered auxiliary processes that may reinforce oxidative stress, whereas the high-entropy catalytic microenvironment remains the key factor governing the amplified redox catalytic activity of HENEs.

Just Accepted

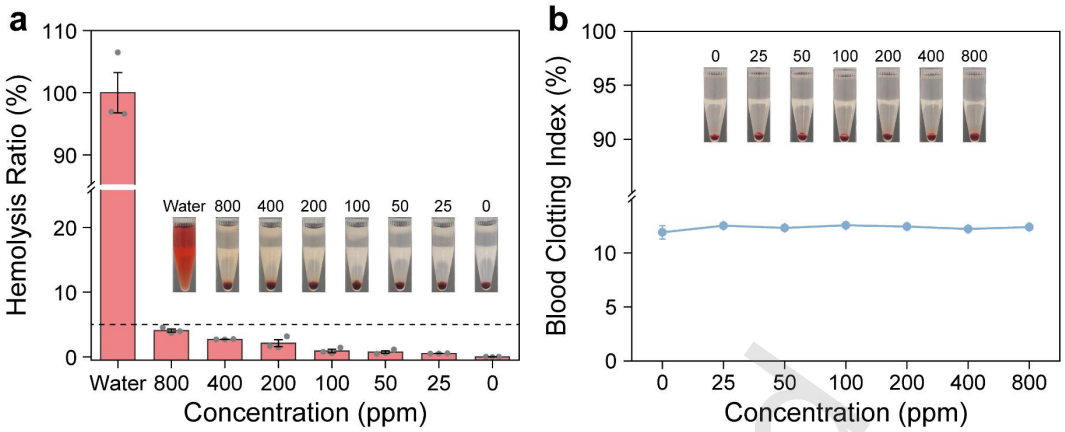


Figure S21. Hemolysis analysis (a) and coagulation analysis (b) of the HENEs treatment group. Data are represented as mean ± s.e.m. from three independent experiments (n = 3).

Just Accepted

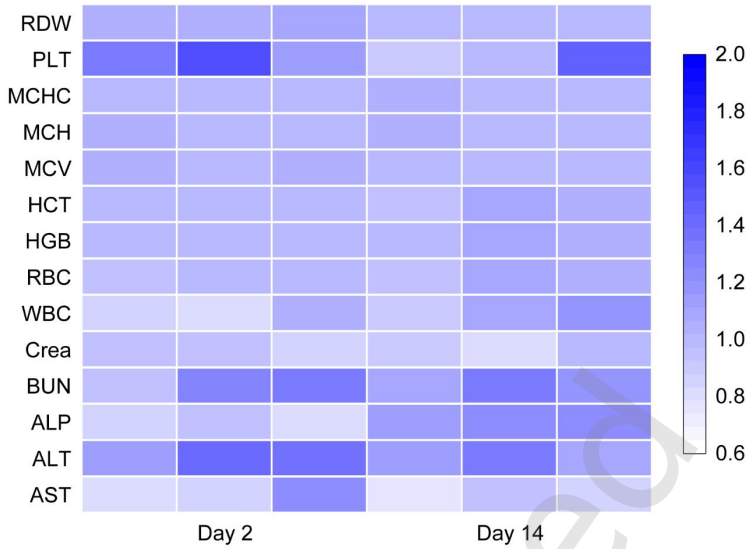


Figure S22. Blood routine and biochemical analyses of HENEs-treated healthy Balb/c mice.

Just Accepted

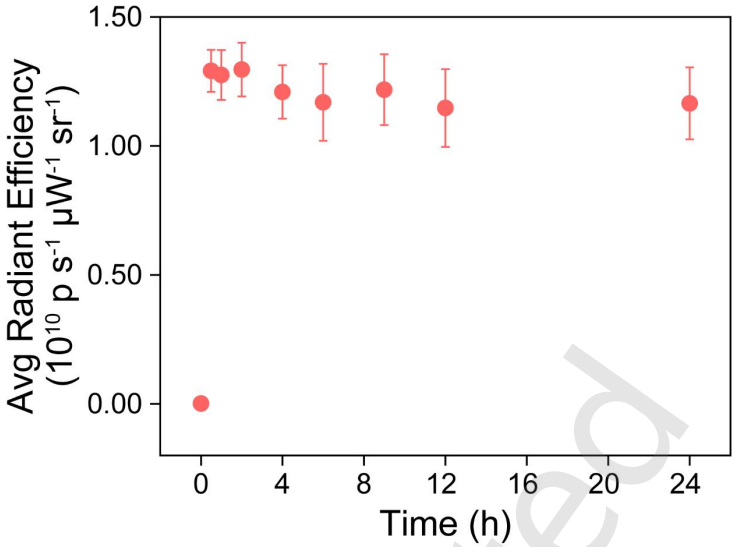


Figure S23. Fluorescence intensity of tumor tissue within 24 h post-administration of HENEs-Cy5.5.

Just Accepted

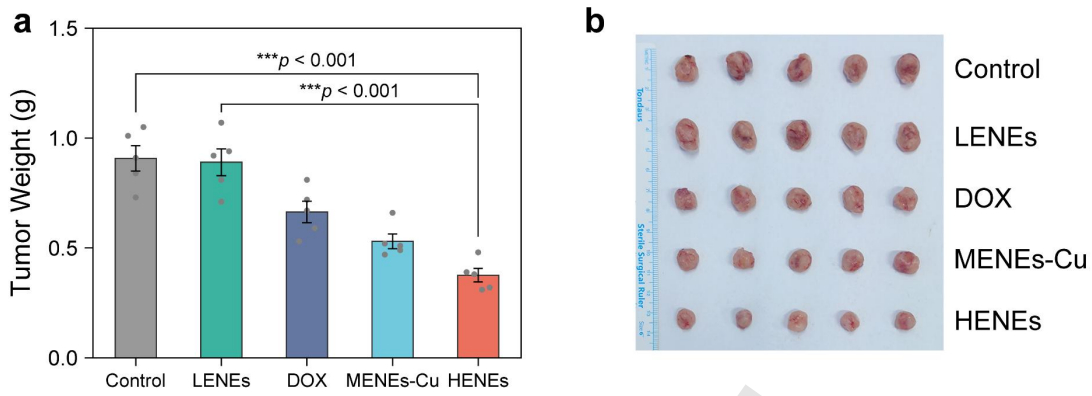


Figure S24. a) Average tumor weight of harvested tumors at the endpoint of treatments from different groups. **b)** Digital photo of harvested tumors at the endpoint of treatment from different groups. Data are represented as mean ± s.e.m. (n = 5).

Just Accepted

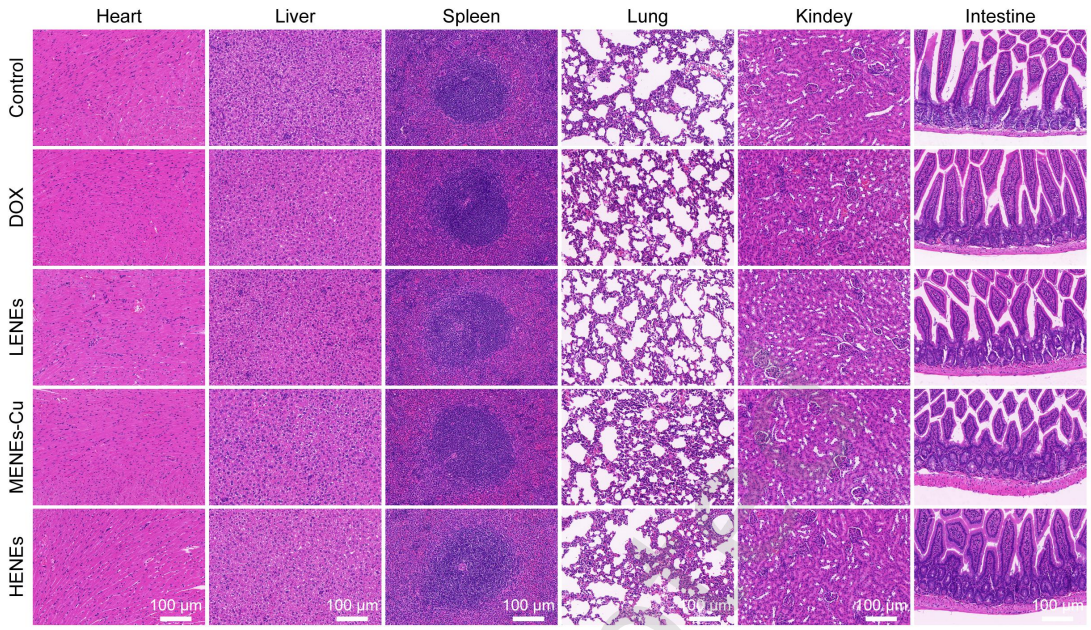


Figure S25. Histological analysis of major organs (heart, liver, spleen, lung, kidney, and intestine) after different treatments.

Just Accepted

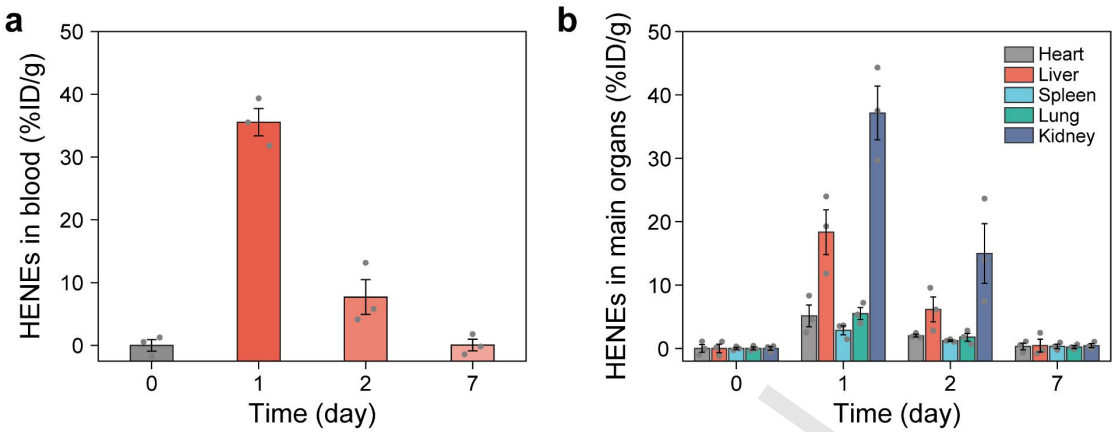


Figure S26. In vivo metabolism analysis of HENEs in blood (a) and main organs (b) within 7 days.

Just Accepted

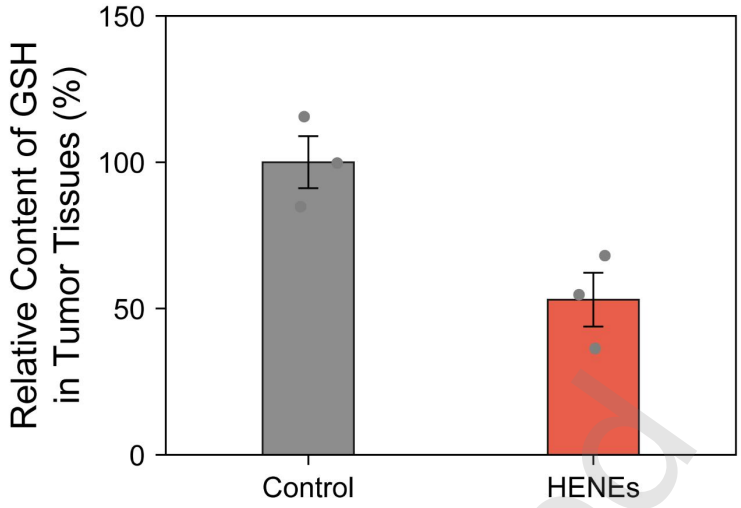


Figure S27. Relative content of GSH in tumor tissues.

Just Accepted

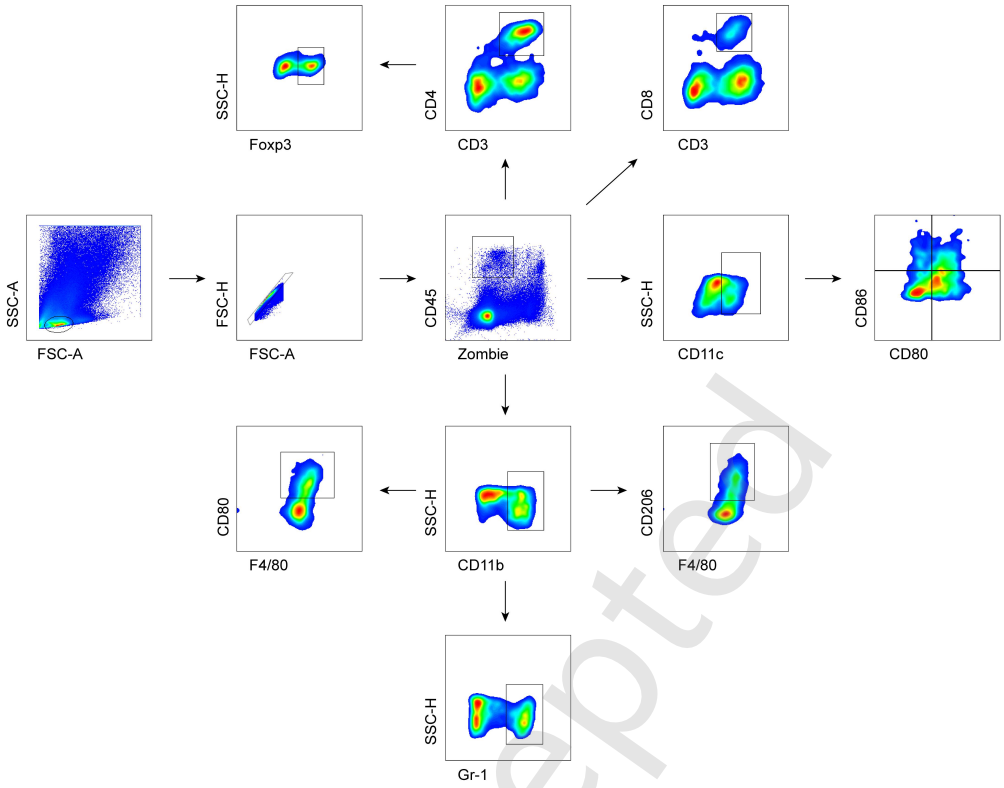


Figure S28. Gating strategies for flow cytometric identification of $CD4^+$ T cells, $CD8^+$ T cells, T_{reg} cells, mature DCs, M1/M2 macrophages, and MDSCs in tumors from 4T1 tumor-bearing mice after each treatment.

Just Accepted

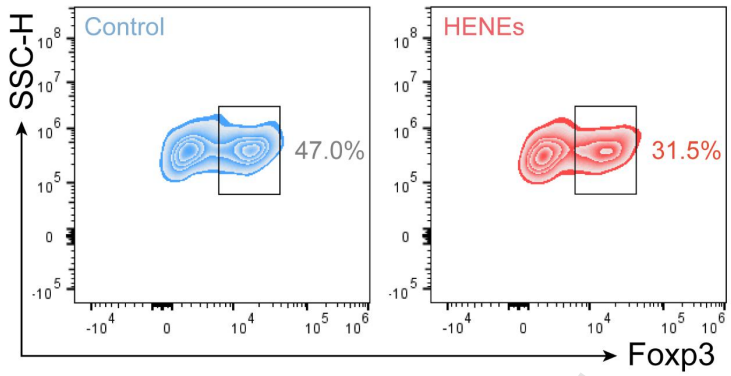


Figure S29. Flow cytometric assay of T_{reg} cells in the tumor.

Just Accepted

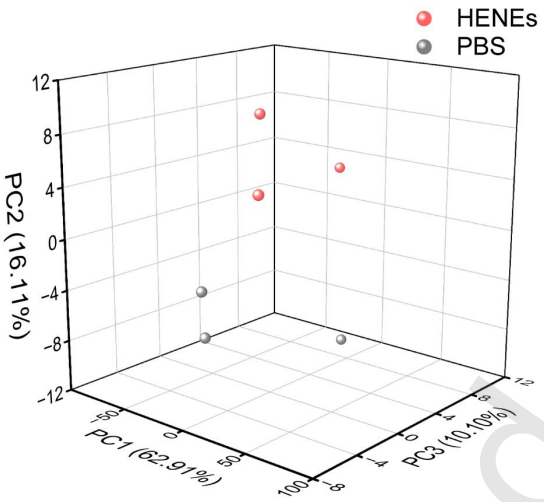


Figure S30. Principal component analysis (PCA) score plot of RNA expression in TME of mice treated with HENEs or PBS (n = 3).

Just Accepted

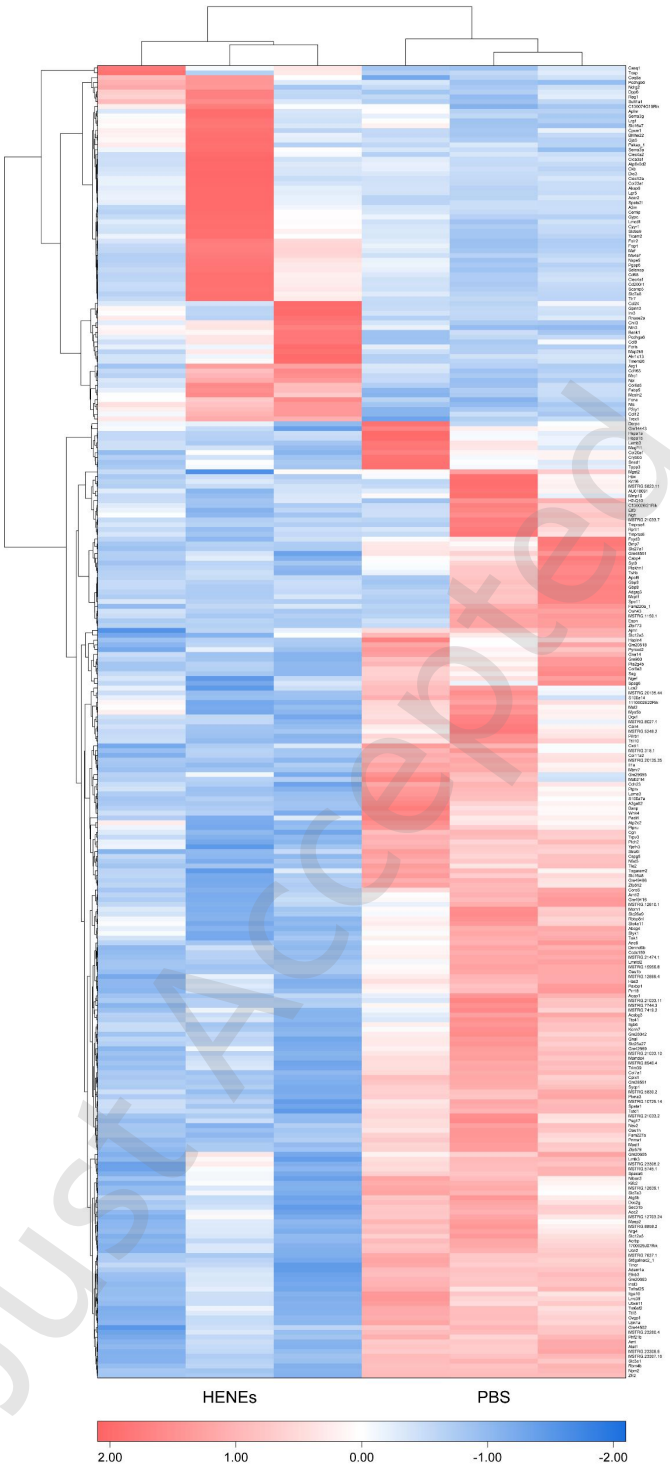


Figure S31. Heat map showing significantly upregulated and downregulated RNA.

Just Accepted

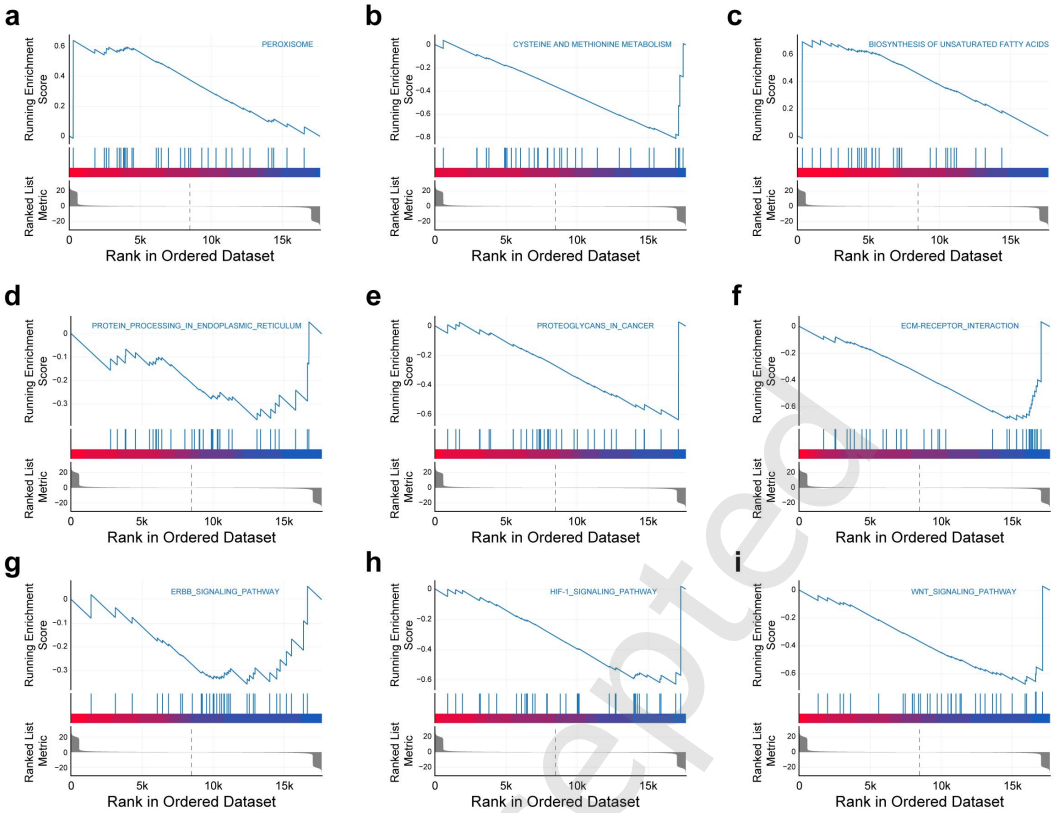


Figure S32. GSEA enrichment analysis of in vivo tumor enzymatic therapy with HENEs. Peroxisome (a). Cysteine and methionine metabolism (b). Biosynthesis of unsaturated fatty acids (c). Protein processing in the endoplasmic reticulum (d). Proteoglycans in cancer (e). ECM-receptor interaction (f). ERBB signaling pathway (g). HIF-1 signaling pathway (h). WNT signaling pathway (i).

Just Accepted

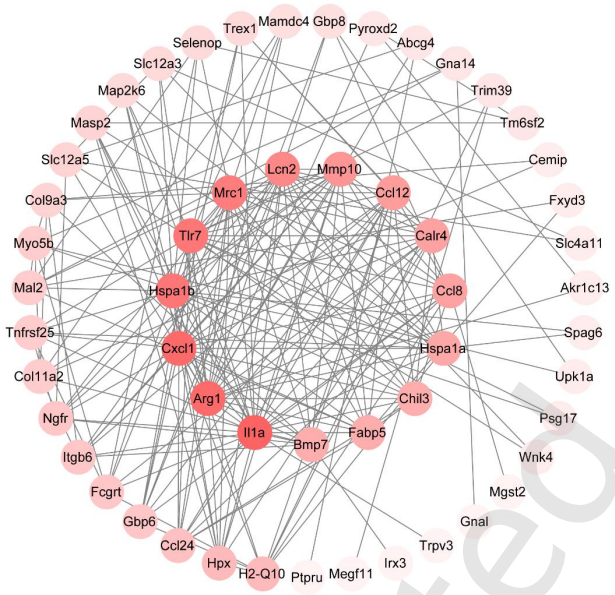


Figure S33. Protein-protein interaction network of DEGs involved in oxidative stress, cell damage, and immune response. The darker the color, the more interactions.

Just Accepted

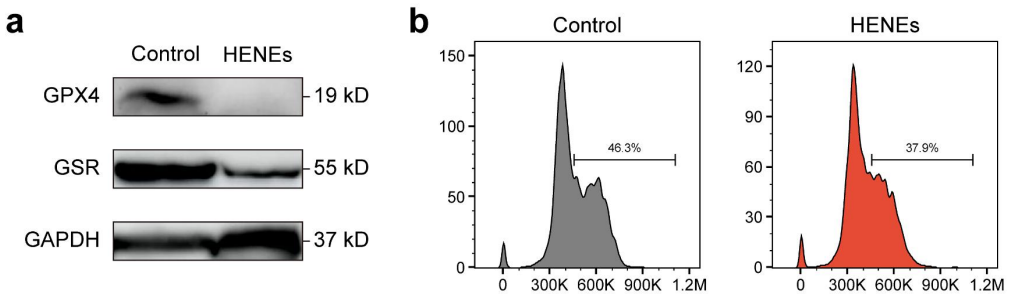


Figure S34. a) Western blot analysis of GSR and GPX4 in 4T1 cells after HENEs treatment, with GAPDH used as the loading control. **b)** Cell cycle arrest assay of HENEs.

Just Accepted